Adaptive multiresolution WENO schemes for multi-species kinematic flow models

Raimund Bürger [a],[*], Alice Kozakevicius [b]

[a] *Departamento de Ingeniería Matemática, Facultad de Ciencias Físicas y Matemáticas, Universidad de Concepción, Casilla 160-C, Concepción, Chile*
[b] *Departamento de Matemática-CCNE, Universidade Federal de Santa Maria, Faixa de Camobi, km 9, Campus Universitário, Santa Maria, RS, CEP 97105-900, Brazil*

Abstract

Multi-species kinematic flow models lead to strongly coupled, nonlinear systems of first-order, spatially one-dimensional conservation laws. The number of unknowns (the concentrations of the species) may be arbitrarily high. Models of this class include a multi-species generalization of the Lighthill–Whitham–Richards traffic model and a model for the sedimentation of polydisperse suspensions. Their solutions typically involve kinematic shocks separating areas of constancy, and should be approximated by high resolution schemes. A fifth-order weighted essentially non-oscillatory (WENO) scheme is combined with a multiresolution technique that adaptively generates a sparse point representation (SPR) of the evolving numerical solution. Thus, computational effort is concentrated on zones of strong variation near shocks. Numerical examples from the traffic and sedimentation models demonstrate the effectiveness of the resulting WENO multiresolution (WENO-MRS) scheme.
© 2006 Elsevier Inc. All rights reserved.

1. Introduction

1.1. Scope of the paper

Numerous multiphase flows in engineering applications involve the flow of one disperse substance, for example solid mineral particles or oil droplets in an emulsion, through a continuous phase, say a liquid or gas. In many cases, the disperse substance consists of small particles that belong to different species differing

---

[*] Corresponding author. Tel.: +56 41 2203126; fax: +56 41 2522055.
E-mail addresses: rburger@ing-mat.udec.cl (R. Bürger), alicek@smail.ufsm.br (A. Kozakevicius).

in some characteristic quantity such as size or density. As a consequence, the disperse substance does not move as one phase; rather, the different species segregate and create areas of different composition. This differential movement of the species is what practitioners in many applications are most interested in, and which is frequently described by spatially one-dimensional models. In most circumstances, the diameter of the particles is small compared to that of the flow duct, which justifies identifying each species with a continuous phase. Our class of models also includes certain continuum approximations of traffic flow of vehicles on a highway if cars with drivers having different preferential velocities are identified as different species.

In general, we distinguish between N different species that give rise to N superimposed continuous phases associated with volume fractions (or, in the case of traffic flow, densities) $\phi_1, \ldots, \phi_N$. If v_i is the phase velocity of species i, then the continuity equations of the N species in differential form are

$$\partial_t \phi_i + \partial_x (\phi_i v_i) = 0, \quad i = 1, \ldots, N, \tag{1.1}$$

where t is time and x is the spatial position (depending on the application, the domain is either bounded or unbounded). The velocities $v_1, \ldots, v_N$ are assumed to be given functions of the vector $\Phi := \Phi(x, t) := (\phi_1(x, t), \ldots, \phi_N(x, t))^{\mathrm{T}}$ of local concentrations. This yields systems of conservation laws of the type

$$\partial_t \phi_i + \partial_x (\phi_i v_i(\Phi)) = 0, \quad i = 1, \ldots, N. \tag{1.2}$$

One-dimensional multi-species flow models given by (1.2), which involve no unknown flow variables other than the concentrations, are called *kinematic*. We are especially interested in two specific models that have attracted recent interest: one of multi-species traffic flow [2,46,49–51] and another of sedimentation of multi-species (so-called *polydisperse*) suspensions [5,11,47,48].

For these and other models, solutions of initial value problems with piecewise constant data and zero-flux or periodic initial-boundary value problems, which are relevant for applications, typically develop discontinuous solutions involving fans of N kinematic shocks separating sectors of constant composition. Consequently, high resolution numerical schemes, which accurately resolve these shocks, are natural candidates for the numerical solution of (1.2). In fact, Wong, Shu and their collaborators [49,51] use weighted essentially non-oscillatory (WENO) schemes for the traffic model, while the first author and collaborators [5,9,10] and Xue and Sun [47] applied central difference schemes [27,34] to the sedimentation model. The novelty of this contribution is a very efficient and accurate scheme for multi-species kinematic flow models by combining the WENO approach with an adaptive multiresolution technique involving a sparse point representation. The resulting method is called *WENO-MRS scheme*. The main objective of our adaptive strategy is to reduce the computational effort in solving systems with a large number of equations, especially when the differential operator is discretized by an expensive upwinding scheme, for example by a WENO scheme. This reduction of effort is mainly achieved via a sparse point representation (SPR) of the numerical solution, which produces savings in terms of flux evaluations in regions where the solution is smooth.

In kinematic flow models, the number N of species may be large. On the other hand, the different species in these applications are competitive. It is therefore convenient to assume a maximal density $\phi_{\max}$ (for example, a maximal "bumper-to-bumper" car density in traffic models or the maximal sphere packing density $\phi_{\max} \approx 0.66$ in sedimentation models), such that the phase space for (1.2) is

$$\mathscr{E}_{\phi_{\max}} := \{ \Phi = (\phi_1, \ldots, \phi_N)^{\mathrm{T}} \in \mathbb{R}^N : \phi_1 \geqslant 0, \ldots, \phi_N \geqslant 0, \phi := \phi_1 + \cdots + \phi_N \leqslant \phi_{\max} \}. \tag{1.3}$$

Introducing the flux vector

$$\mathbf{f}(\Phi) = (f_1(\Phi), \ldots, f_N(\Phi))^{\mathrm{T}} := (\phi_1 v_1(\Phi), \ldots, \phi_N v_N(\Phi))^{\mathrm{T}}, \tag{1.4}$$

we can rewrite (1.2) as the nonlinear system of conservation laws

$$\partial_t \Phi + \partial_x \mathbf{f}(\Phi) = 0. \tag{1.5}$$

Solutions of (1.5) are discontinuous in general, and the propagation speed $\sigma(\Phi^+, \Phi^-)$ of a discontinuity in ϕ_i separating the states Φ^+ and Φ^- satisfies the well-known Rankine–Hugoniot condition

$$\sigma = \frac{f_i(\Phi^+) - f_i(\Phi^-)}{\phi_i^+ - \phi_i^-}. \tag{1.6}$$

We recall that the system (1.5) is called *hyperbolic* at a state Φ if the Jacobian $\mathscr{J}_{\mathbf{f}}(\Phi) := (\partial f_i/\partial \phi_k)_{1 \leqslant i,k \leqslant N}$ only has real eigenvalues, and *strictly hyperbolic* if these are moreover pairwise distinct. For $N = 2$, a system with a pair of complex conjugate eigenvalues is *elliptic*. In some circumstances, the type is *mixed*, which means that the system is non-hyperbolic (or elliptic) for all $\Phi \in E \subset \mathscr{E}_{\phi_{max}}$ and $\mathscr{E}_{\phi_{max}} \backslash E \neq \varnothing$. For $N \leqslant 3$, the ellipticity criterion can be evaluated by a convenient calculation of a discriminant [11].

1.2. Multi-species kinematic models

The kinematic traffic model for $N = 1$ goes back to Lighthill and Whitham [30] and Richards [35]; for the sedimentation of suspensions, the classic reference is Kynch [28]. The extension of the Lighthill–Whitham–Richards (LWR) model to multi-class traffic flow was proposed independently by Wong and Wong [46] and Benzoni-Gavage and Colombo [2], while analogous extensions of the sedimentation model have been suggested for several decades (see [9,48] for reviews), mainly in the chemical engineering literature. Though the kinematic models fall within the mainstream research area of systems of conservation laws [16,29], the application of available tools of mathematical and numerical analysis is difficult. This is largely due to the dependence of the functions $v_i(\Phi)$ on all variables $\phi_1, \ldots, \phi_N$, which in general is nonlinear. For Φ from the interior of $\mathscr{E}_{\phi_{max}}$, $\mathscr{J}_{\mathbf{f}}(\Phi)$ usually has nonzero entries only, such that closed formulas for its eigenvalues and eigenvectors are at least complicated, and in general unavailable for $N \geqslant 5$. It is therefore in general not possible to solve the Riemann problem for (1.2) in closed form. This contrasts with what is known for many systems of conservation laws representing balances of different variables (for example, mass, linear momentum and energy) of a single-phase flow, such as the Euler equations of gas dynamics. Moreover, for multi-species kinematic flow models eigenvalues lack a direct physical interpretation, and in particular do not coincide with any of the phase velocities $v_1, \ldots, v_N$. (In contrast to this, the eigenvalues for the Euler equations of gas dynamics are the velocity of the gas, and the velocity plus or minus sound speed.)

Most published solution constructions for multi-species kinematic flow models are based on simplifications. For example, Greenspan and Ungarish [21] and Schneider et al. [38] solve the problem of settling of an N-disperse, initially homogeneous suspension with equal-density particle species under the assumption that solutions exclusively consist of areas of constant composition (excluding continuous variations) that are separated by straight, possibly intersecting kinematic shocks whose speeds are determined by the Rankine–Hugoniot condition. Unfortunately, this construction violates Liu's entropy condition (see [16]), as is most easily seen for $N = 1$, where solutions do not agree with the well-established theory for a scalar conservation law. In fact, some of the kinematic shocks constructed in [21,38] should be replaced by rarefaction waves. For the case $N = 2$, correct solutions including rarefaction waves were constructed by Fried and Roy [20]. The simplification applied in [20] is the choice of the functions $v_i(\Phi) = c_i(1 - \phi)$ for $i = 1, 2$, where $c_i > 0$ are constants. The resulting equations do not exhibit linear degeneracy, a property that facilitates the discussion if compared to the case, for example, that the factor $(1 - \phi)$ is replaced by $(1 - \phi)^n$ with $n > 1$; this is the case more relevant to practice. A full solution construction of the latter case for $N = 2$, which obeys Liu's entropy principle, is given in [4]. However, the result does not appear in closed or implicit form; rather, certain trajectories have to be determined by numerical integration of ordinary differential equations.

While exact solution constructions remain difficult, great advances were made recently in the hyperbolicity analysis and characterization of eigenvalues of multi-species kinematic models. For a model of settling of oil-in-water dispersions, which is similar to the sedimentation and traffic models, Rosso and Sona [36] proved for arbitrary N strict hyperbolicity in the interior of $\mathscr{E}_{\phi_{max}}$. The proof is based on deriving an explicit closed formula of the characteristic polynomial $p(\lambda; \Phi) = \det(\mathscr{J}_{\mathbf{f}}(\Phi) - \lambda \mathbf{I})$ by exploiting elimination possibilities in the determinant. Then $p(\lambda; \Phi)$ is evaluated at N suitable λ-arguments that produce values of alternating sign, which along with a discussion of $p(\lambda; \Phi)$ for $\lambda \to \pm \infty$ implies that $p(\lambda; \Phi)$ must have N distinct zeros. After preliminary analyses for $N \leqslant 3$ [11], Berres et al. [5] proved in a similar way that the Masliyah–Lockett–Bassoon (MLB) model [5,31,32] for sedimentation of polydisperse suspensions with equal-density particles is strictly hyperbolic for an arbitrary number N of species (size classes). The basic idea was also used by Zhang et al. [50] to prove strict hyperbolicity of the multi-class traffic model proposed in [2,46].

1.3. High resolution and multiresolution schemes

High resolution schemes for conservation laws are of at least second-order accuracy in regions where the solution is smooth, and on the other hand resolve discontinuities sharply and without spurious oscillations. Methods of this type include essentially non-oscillatory (ENO) schemes (see [40]) and central and total variation diminishing (TVD) schemes [27,34]; see also the references cited in these papers and [29,43]. Clearly, resolution is gained by these methods at increased computational cost, especially for systems of conservation laws, more than one space dimension, a large number of points in the computational grid, or extended simulation times.

In light of Section 1.2, insight into an N-species kinematic flow model with $N \geqslant 3$ can realistically be gained through numerical simulation only. On the other hand, N different characteristic speeds will produce solutions of Riemann problems with a fan of up to N shocks or rarefactions which separate areas of constant composition. High resolution schemes that have been applied to multi-species kinematic models include WENO schemes [49,51] and central difference schemes, such as the Kurganov–Tadmor [27] and Nessyahu–Tadmor [34] schemes [5,9,10,47]. We herein pursue the WENO approach, and show that the multiresolution technique applied to WENO schemes together with a sparse point representation (SPR) leads to an efficient and accurate scheme for multi-species kinematic flow models.

The multiresolution method has been devised (at least, originally) to reduce the computational cost of high resolution methods. In standard situations, the solution of a conservation law exhibits strong variations (shocks) in small regions but behaves smoothly on the major portion of the computational domain. The multiresolution technique adaptively concentrates computational effort on the regions of strong variation. It goes back to Harten [22] for hyperbolic equations and was used by Bihari [7] and Roussel et al. [37] for parabolic equations. Multiresolution methods for conservation laws in several space dimensions are analyzed by Dahmen et al. [17], while fully adaptive multiresolution finite volume schemes, including an optimized adaptive memory storage, are presented by Cohen et al. [15]. See Chiavassa et al. [14] for a recent review on multiresolution methods for hyperbolic conservation laws.

Adaptive methods can be separated into two classes: one based on grid refinement to resolve gradients of a physically relevant quantity (see e.g. [24,25]), the other based on a posteriori error estimators, see e.g. [3] and the references therein. The present paper belongs to the first of these classes.

Nonorthogonal or orthogonal wavelets are an efficient tool in developing adaptive numerical methods from both classes [8,12,13,17,22,37]. Interpolating wavelets [18,23] are efficiently combined with linear or nonlinear thresholding strategies in order to produce sparse approximations on a near optimal grid. It is this family of wavelets that are used in this paper.

1.4. Contents of the paper

The remainder of this paper is organized as follows. Section 2 presents the WENO-MRS method. To this end, we recall in Sections 2.1 and 2.2 the multiresolution representation of a function on a sequence of nested dyadic grids, which generates a sequence of details or wavelet coefficients. It is also recalled how these details encode information on the smoothness of a given original function, and how discarding sufficiently small details, the so-called thresholding operation, can be used for data compression. This leads to an SPR of the function on a sparse grid. The necessity of introducing safety points, that is, additional points near significant details, is set out in Section 2.3. The available algorithm by Harten [22] to generate the required index set of significant positions is then recalled (Algorithm 2.1). Moreover, we specify in Algorithm 2.2 how the SPR of the numerical solution is updated in each time step. In Section 2.4 we describe the TVD Runge–Kutta scheme employed for the time discretization of (1.5), while Section 2.5 outlines the WENO scheme applied to the SPR of the solution. Section 2.6 summarizes the resulting WENO-MRS scheme in Algorithm 2.3. This algorithm is presented for zero-flux boundary conditions and a finite domain; the small changes necessary for periodic boundary conditions are addressed in Section 2.7.

In Section 3, three different multi-species kinematic flow models are presented. Section 3.1 presents the multi-class kinematic traffic model, which gives rise to an initial value problem with periodic boundary conditions. Next, in Section 3.2, we outline the polydisperse sedimentation model, for which the zero-flux

boundary condition is relevant. A similar model for the separation of oil-in-water dispersions is mentioned in Section 3.3. Though the model is developed in a slightly different way than the sedimentation model, the final equations are equivalent, so no solutions are presented for the dispersion model.

Finally, Section 4 presents six different numerical examples illustrating the performance of the WENO-MRS method. Examples 1 and 2, which form Section 4.1, have been adapted from [49] and are related to the traffic model, while Examples 3–6, presented in Section 4.2, have been taken from the sedimentation model.

2. Multiresolution methods

2.1. Multiresolution framework

Let $(G^0, G^1, \ldots, G^{L_c})$ denote a family of uniform nested grids on the interval $I := [a, b]$, where $G^0 := (x_0^0, x_1^0, \ldots, x_{N_0}^0)$, $N_0 = 2^m$, $m \in \mathbb{N}$ is the finest one (the finest resolution level) and $h_0 := (b - a)/N_0$ is the finest cell length. The values of a function u on G^0 are the input data. The remaining dyadically coarsened grids are obtained in the following recursive way: given a grid G^{k-1}, we obtain the next coarsest grid G^k by removing the even-indexed grid points. Therefore $G^{k-1} \setminus G^k = (x_{2j-1}^{k-1})_{j=1,\ldots,N_k}$, $G^{k-1} \cap G^k = G^k$ and $x_j^k = x_{2j}^{k-1}$ for $0 \leqslant j \leqslant N_k = 2^{m-k}$, $k = 1, \ldots, L_c$. Due to the embedding of the grids, the representation of u on any coarser grid G^k, $k = 1, \ldots, L_c$ can be obtained directly from the finest level $k = 0$: $u_j^k = u(x_j^k) = u(x_{2^k j}^0) = u_{2^k j}^0$ for $0 \leqslant j \leqslant N_k$. To recover the representation of u on G^{k-1} from its representation on the next coarser grid G^k, we need an interpolation operator $\mathscr{I}(u^k, x)$ of u on G^k to obtain approximations for the missing points of G^{k-1}. The function value at x_{2j-1}^{k-1} is obtained from the $(r-1)$th degree polynomial interpolating the $r = 2s$ consecutive points $(u_{j-s}^k, \ldots, u_{j+s-1}^k)$. Therefore

$$\tilde{u}_{2j-1}^{k-1} = \mathscr{I}(u^k, x_{2j-1}^{k-1}) = \sum_{l=1}^{s} \beta_l (u_{j+l-1}^k + u_{j-l}^k), \quad r = 2s, \text{ with } \begin{cases} \beta_1 = 1/2 & \text{for } r = 2, \\ \beta_1 = 9/16, \ \beta_2 = -1/16 & \text{for } r = 4. \end{cases}$$

(2.1)

When the function is non-periodic, the stencil of interpolation is modified in order to consider all points inside the domain. In this case, and for $r = 4$, the following interpolator is specified (instead of (2.1)):

$$\mathscr{I}(u^k, x_{2j-1}^{k-1}) = \frac{1}{16} \cdot \begin{cases} 5u_0^k + 15u_1^k - 5u_2^k + u_3^k & \text{for } j = 1, \\ -u_{j-2}^k + 9u_{j-1}^k + 9u_j^k - u_{j+1}^k & \text{for } j = 2, \ldots, N_k - 1, \\ u_{N_k-3}^k - 5u_{N_k-2}^k + 15u_{N_k-1}^k + 5u_{N_k}^k & \text{for } j = N_k. \end{cases}$$

(2.2)

The interpolation errors, known as *details* or *wavelet coefficients*, are $d_j^k := u_{2j-1}^{k-1} - \tilde{u}_{2j-1}^{k-1}$ for $1 \leqslant j \leqslant N_k$. Thus, with the knowledge of $u^k := (u_0^k, u_1^k, \ldots, u_{N_k}^k)$ and $d^k := (d_0^k, d_1^k, \ldots, d_{N_k}^k)$, we can exactly recover the representation of u on G^{k-1}. The pair of vectors (u^k, d^k) is the *multiresolution representation* of u^{k-1}. Applying successively this procedure for $1 \leqslant k \leqslant L_c$, we can recover the values of u on the finest level of resolution from its values on the coarsest level L_c and the sequence of all details from levels L_c to 1:

$$u^0 \leftrightarrow (d^1, u^1) \leftrightarrow (d^1, d^2, u^2) \leftrightarrow \cdots \leftrightarrow (d^1, d^2, \ldots, d^{L_c}, u^{L_c}) =: u_M,$$

(2.3)

where u_M is the *multiresolution representation* of $u^0 \equiv u$. The details d^k contain information on the smoothness of u, and will be used to flag the non-smooth parts of the solution in the adaptive numerical method.

These flags are utilized to generate a sparse numerical grid for the approximation of the solution in each time step. To motivate this technique, we recall in Section 2.2 some results of the underlying regularity analysis and the thresholding operation. In Section 2.3, we first briefly review the known construction of an SPR for a scalar function, and then explain how the sparse grid $\overline{\Gamma}$ for each time step is built from the sets of significant positions for each of the N components of the vector-valued function u. This set is calculated by a version of Harten's algorithm [22] for the scalar case (our Algorithm 2.1 in Section 2.3). This algorithm forms the core of our Algorithm 2.2, which describes how the SPR is updated in each time step.

2.2. Regularity analysis

Standard interpolation results imply that if u at a point x has $p - 1$ continuous derivatives and a jump discontinuity in its pth derivative, then for x_j^k near x,

$$d_j^k \sim \begin{cases} (h_k)^p [u^{(p)}] & \text{for } 0 \leqslant p \leqslant \bar{r}, \\ (h_k)^{\bar{r}} u^{(\bar{r})} & \text{for } p > \bar{r}, \end{cases} \tag{2.4}$$

where $h_k := (b - a)/N_k$, $\bar{r} := (r - 1) + 1 = r$ is the order of accuracy of the approximation, and $[\cdot]$ denotes the jump at the discontinuity. Therefore $|d_{2j}^{k-1}| \approx 2^{-\bar{p}} |d_j^k|$, if the kth level is fine enough, where $\bar{p} := \min\{p, \bar{r}\}$. Thus, away from discontinuities of u, the wavelet coefficients d_j^k diminish as the levels of resolution become finer, at a rate which is determined by the local regularity of u and the order of accuracy of the approximation. In the neighborhood of a discontinuity of the function, the details remain of the same size for all levels of refinement.

Multiresolution schemes achieve data compression, and reduction of computational effort, by considering only details d_j^k that are larger in absolute value than a certain level-dependent comparison value ε_k to be significant. This means that one computes the quantities

$$\hat{d}_j^k := \text{tr}_{\varepsilon_k}(d_j^k) := \begin{cases} 0 & \text{if } |d_j^k| < \varepsilon_k, \\ d_j^k & \text{if } |d_j^k| \geqslant \varepsilon_k, \end{cases} \quad 1 \leqslant j \leqslant N_k, \ 1 \leqslant k \leqslant L_c, \tag{2.5}$$

where $\text{tr}_{\varepsilon_k}$ is the so-called *thresholding* or *truncation operator* with the level-dependent *threshold parameters* ε_k, $1 \leqslant k \leqslant L_c$. The computation of $\hat{d}_j^k = \text{tr}_{\varepsilon_k}(d_j^k)$ is called *thresholding* or *truncation*.

For a function u that has been generated by a numerical scheme, the number $\bar{p}$ is difficult to define. In the numerical examples presented herein, we use the thresholding strategies $\varepsilon_k = 2\varepsilon_{k-1}$ or $\varepsilon_k = 2.5\varepsilon_{k-1}$, along with a set value of ε_0, where the factor 2 or 2.5 "estimates" the factor $2^{\bar{p}}$ at level k. Our choice of these strategies is also based on experience with a version of the multiresolution method for scalar degenerate parabolic equations for similar models [12], and has turned out to provide a good compromise between data compression and preservation of relevant information. Furthermore, we utilize a parameter θ_k which measures the lack of regularity in the details near numerically detected jump in some derivative of u. This parameter appears as a threshold for comparison in Algorithms 2.1 and 2.2, and controls how positions on the next finer grid (on level $k - 1$) near a discontinuity are marked. Therefore, if used to mark a significant position on level $k - 1$, $|d_j^k|$ should be consistently compared with ε_k multiplied by the factor that is used to estimate $2^{\bar{p}}$. We therefore utilize $\theta_k = 2\varepsilon_k$ and $\theta_k = 2.5\varepsilon_k$, respectively.

In our case, the result of the thresholding operation is a set of markers (Boolean flags) that indicate whether $|d_j^k| > \varepsilon_k$ or not, that is, whether a position (j, k) in the multiresolution is significant or not. (The computation of this set of markers is formalized in Algorithms 2.1 and 2.2 below.) This information controls whether a point value of u is included in the SPR of u or not.

2.3. Sparse point representation

The SPR of a function u is associated to a sparse grid $\overline{\Gamma}$ with $G^{L_c} \subset \overline{\Gamma} \subset G^0$, and consists of all exact point values of u that correspond to positions belonging to $\overline{\Gamma}$. The set $\overline{\Gamma}$ consists of all positions that are judged significant according to the thresholding operation (2.5), plus all point values of the coarsest grid, and certain safety points (this is made precise below). To build the SPR, we use a sparse data structure, storing in one vector sequentially the point values of significant positions of u^0 and in another the corresponding positions with respect to the finest uniform grid G^0. These vectors are obtained after the construction of an index set, called $\overline{\mathscr{D}}$, that flags whether a detail is significant. Therefore, $\overline{\Gamma}$ is the set of grid points flagged by $\overline{\mathscr{D}}$.

Whenever needed for flux evaluations, values corresponding to positions not contained in the SPR are interpolated from solution values belonging to the SPR. In other words, values of positions not belonging to the SPR can be discarded, so that the SPR presents a way of using the compression capabilities of multiresolution representations. The compression effect due to the computation can be quantified by the number of details contained in the SPR, denoted N_s. Of course, for a given function u, N_s depends substantially on the choice of the thresholding strategy, that is, the sequence of values ε_k, $k = 1, \dots, L_c$.

Several variants of multiresolution methods applied to solving a differential equation differ in the evaluation of the differential operator. This evaluation can be performed either on the SPR as a collocation method or by finite differencing on $\overline{\Gamma}$ [24–26], or on the uniform fine grid, keeping the entire (non-sparse) representation of $\tilde{u}^0$ but adapting the manner in which the flux is calculated to the significant positions [7,12,13,22]. In this work we pursue the first approach and adapt a WENO scheme to evolve the solution to the non-equidistant sparse grid $\overline{\Gamma}$ via the concept of local scale [24]. Clearly, we need to update the SPR of after each time step of the numerical solution, which is described in Algorithm 2.2.

In each time step, the SPR has to be able to represent and to capture the finite speed of propagation of information and the formation of shock waves. For this reason, Harten [22] proposed to include *safety points* near significant positions (for which $|d_j^k| \geqslant \varepsilon_k$). Due to these safety points, the sparse grid correctly detects the formation of shocks and their development.

The SPR of the vector-valued solution of (1.5) is based on the union of the SPRs of each of the N vector components. To obtain the unified representation, we first compute index sets $\overline{\mathscr{D}}^i$, $i = 1, \ldots, N$, each for one component, that include the positions of the significant coefficients and the positions of safety points, and then define the index set $\overline{\mathscr{D}} := \overline{\mathscr{D}}^1 \cup \cdots \cup \overline{\mathscr{D}}^N$. Then we build an SPR for each vector component with respect to $\overline{\Gamma}$, which is the set of grid points from $\overline{\mathscr{D}}$ plus all points from the coarsest level, i.e. we define

$$\overline{\Gamma} := \{x_{2j-1}^{k-1} | \ (j,k) \in \overline{\mathscr{D}}\} \cup \{x_0^{L_c}, \ldots, x_{L_c}^{L_c}\} = \bigcup_{i=1}^{N} \{x_{2j-1}^{k-1} | \ (j,k) \in \overline{\mathscr{D}}^i\} \cup \{x_0^{L_c}, \ldots, x_{L_c}^{L_c}\}, \tag{2.6}$$

and $N_s := \#\overline{\Gamma}$. We here recall Harten's algorithm [22], which leads to the set $\overline{\mathscr{D}}^i$ for one component $i \in \{1, \ldots, N\}$. We only perform the algorithm for the entire dyadic grid positions in the first iteration. After that, we visit only points from an existing SPR in order to update it (see Algorithm 2.2). As mentioned in Section 2.2, a parameter θ_k controls the addition of safety points on finer scales, and ε_k is the threshold value.

Since in the course of the WENO-MRS scheme, Algorithm 2.1 is used only once, namely to calculate the SPR of one of the components of the initial vector

$$\Phi(x,0) = \Phi_0(x) := (\phi_{1,0}(x), \ldots, \phi_{N,0}(x))^{\mathrm{T}}, \quad \Phi_0(x) \in \mathscr{E}_{\phi_{\max}},$$

the input data for Algorithm 2.1 is the complete multiresolution representation (2.3) of the fine-grid representation $u^0 := (\phi_{i,0}(x_0^0), \phi_{i,0}(x_1^0), \ldots, \phi_{i,0}(x_{N_0}^0))$ for a fixed value of the index i, $i \in \{1, \ldots, N\}$.

Algorithm 2.1.

1. Set flags: $\hat{i}(j,k) \leftarrow 0$, $1 \leqslant j \leqslant N_k$, $1 \leqslant k < L_c$, $\hat{i}(j, L_c) \leftarrow 1$, $1 \leqslant j \leqslant N_{L_c}$.
2. Thresholding and extension:
    do $k = 1, \ldots, L_c$
        do $j = 1, \ldots, N_k$
            if $|d_j^k| \geqslant \varepsilon_k$ **then**
                $\hat{i}(m,k) \leftarrow 1$, $m = j-1, j, j+1$
                if $|d_j^k| \geqslant \theta_k$ **and** $k > 1$ **then**
                    $\hat{i}(2j-1, k-1) \leftarrow 1$, $\hat{i}(2j, k-1) \leftarrow 1$
                endif
            endif
        enddo
    enddo
3. $\overline{\mathscr{D}}^i := \{(j,k) | \hat{i}(j,k) = 1\}$.

In the second and all subsequent time steps of the WENO-MRS method, we need to update the SPR from the respective previous time step. To obtain a new SPR after a time iteration is completed (here, a TVD Runge–Kutta cycle), we utilize an algorithm proposed in [24], which performs the wavelet transform only for those points that correspond to significant positions, i.e. positions in $\overline{\mathscr{D}}$. To compute the predictor, if any point value is needed that is not included at the sparse point representation, the value is recursively interpolated from a coarser scale. The algorithm will terminate, since all function values of the coarsest grid belong

to the SPR at any time step. After this sparse wavelet transform, the thresholding and extension operations are performed as in Algorithm 2.1 in order to update the flags. New point values to be included in the SPR are obtained in the same way by interpolation from coarser levels.

After each time step, this process is repeated: new details are computed, new flags are determined and according to the new flags, positions are included on or excluded from the updated sparse grid. In the case of inclusion, interpolated point values are associated to the new grid position. According to [3], one could keep the same grid configuration for more than one time step, and then execute the necessary update. The number of time steps during which a grid is kept unaltered is associated with the speed of wave propagation.

We assume that Algorithm 2.2 is applied to new solution values $\phi_i^n(x_j^k) \approx \phi_i(x_j^k, t_n)$ for $(j,k) \in \overline{\mathscr{D}} \subset \overline{\Gamma}$, $i = 1, \ldots, N$, where $\overline{\Gamma}$ is the sparse grid of the old SPR. In other words, it is assumed that the update of the solution from t_{n-1} to t_n has been performed on $\overline{\Gamma}$. Algorithm 2.2 then applies to one selected component $i \in \{1, \ldots, N\}$, such that the input data are $\{u_j^k := \phi_i^n(x_j^k) : (j,k) \in \overline{\Gamma}\}$.

Algorithm 2.2.

1. Local wavelet transform:
    do $k = L_c, \ldots, 1$
      for $(j,k) \in \overline{\mathscr{D}}$
        Compute the predictor $\tilde{u}_{2j-1}^{k-1}$ and the detail $d_j^k = u_{2j-1}^{k-1} - \tilde{u}_{2j-1}^{k-1}$
      endfor
    enddo
2. Thresholding, extension and inclusion of a point into the SPR:
    do $k = 1, \ldots, L_c$
      for $(j,k) \in \overline{\mathscr{D}}$
        if $|d_j^k| \geqslant \varepsilon_k$ **then**
          include missing neighbors into the SPR:
          $\hat{i}(m,k) \leftarrow 1$, $m = j-1, j, j+1$
          if $|d_j^k| \geqslant \theta_k$ **and** $k > 1$ **then**
            $\hat{i}(2j-1, k-1) \leftarrow 1$, $\hat{i}(2j, k-1) \leftarrow 1$
          endif
        else
          $\hat{i}(j,k) \leftarrow 0$
        endif
      endfor
    enddo
3. $\overline{\mathscr{D}}^i := \{(j,k) | \hat{i}(j,k) = 1\}$.

Once updated versions of all sets $\overline{\mathscr{D}}^1, \ldots, \overline{\mathscr{D}}^N$ are available, the new sparse grid $\overline{\Gamma}$ is defined by (2.6).

Let us also comment that for certain applications, it is sufficient to inspect the details of one scalar variable (for example, density in gas dynamics) rather than of all components (as we do) to determine the set of significant positions. Clearly, this would accelerate the computation of the SPR, which is done here by an N-fold application of Algorithms 2.1 and 2.2. However, kinematic flow models include situations in which there is a complete spatial segregation of species (which is especially likely to occur in the traffic model), so that one scalar component cannot be used as a smoothness indicator. One quantity that potentially could capture all discontinuities of the individual densities ϕ_1 to ϕ_N is the global density $\phi = \phi_1 + \cdots + \phi_N$. Nevertheless, for these models ϕ does not appear to be a smoothness indicator, for reasons we briefly discuss in Section 4.2.4 in light of numerical results for Example 6.

2.4. Time discretization

For the time discretization of the sample system $\partial_t \Phi = \mathscr{L}(\Phi) \equiv -\partial_x \mathbf{f}(\Phi)$, we utilize the general class of explicit n_{RK}-step TVD Runge–Kutta schemes (see [40])

$$\Phi_j^{(0)} := \Phi_j^n, \quad \Phi_j^{(i)} := \sum_{k=0}^{i-1}(\alpha_{ik}\Phi_j^{(k)} + \Delta t\beta_{ik}\mathscr{L}_j(\Phi^{(k)})), \quad i = 1, \ldots, n_{\mathrm{RK}}, \quad \Phi_j^{n+1} := \Phi_j^{(n_{\mathrm{RK}})}. \tag{2.7}$$

The scheme is characterized by the coefficients α_{ik} and β_{ik}, which need to satisfy $\alpha_{ik} \geqslant 0$, $\alpha_{i0} + \cdots + \alpha_{i,i-1} = 1$ for $i = 1, \ldots, n_{\mathrm{RK}}$, and certain additional conditions to ensure the TVD property.

We limit ourselves here to the zero-flux initial-boundary value problem for (1.2); in this case it is convenient to distinguish between the interior operators $\mathscr{L}_1, \ldots, \mathscr{L}_{N_0-1}$ and the boundary operators $\mathscr{L}_0$ and $\mathscr{L}_{N_0}$, which result from including the boundary conditions in the fully discrete version. The scheme used specifically in this paper is the of TVD Runge–Kutta scheme of order and step number $n_{\mathrm{RK}} = 3$:

$$\Phi_j^{(1)} = \Phi_j^n + \Delta t\mathscr{L}_j(\Phi^n), \quad \Phi_j^{(2)} = \frac{1}{4}\left(3\Phi_j^n + \Phi_j^{(1)} + \Delta t\mathscr{L}_j(\Phi^{(1)})\right),$$
$$\Phi_j^{n+1} = \frac{1}{3}\left(\Phi_j^n + 2\Phi_j^{(2)} + 2\Delta t\mathscr{L}_j(\Phi^{(2)})\right), \quad j = 0, \ldots, N_0, \ n = 0, 1, 2, \ldots. \tag{2.8}$$

2.5. Space discretization

We assume that the SPR of the numerical solution to be advanced over the next time step is already built either by Algorithm 2.1 (for the first time step) or Algorithm 2.2 (for all other time steps). Point values of the initial solution of (1.2) are given on a uniform fine grid G^0, and the corresponding SPR is considered already built, where the sparse grid is denoted by $\overline{\Gamma}$. To simplify notation, we denote in this section by $\bar{\Phi} = (\bar{\phi}_1, \ldots, \bar{\phi}_N)^{\mathrm{T}}$ solution vectors belong to the SPR. (We recall that the SPR is unified in the sense that the sparse representation is the same for all species.) The numerical fluxes that determine the evolution of (1.2) will be calculated on $\overline{\Gamma}$. A conservative semi-discrete approximation $\overline{\Phi}_i(t) = (\bar{\phi}_{1,i}(t), \ldots, \bar{\phi}_{N,i}(t))^{\mathrm{T}}$ to the exact solution $\bar{\Phi}(x_i, t)$ of (1.5) satisfies the system of ODEs

$$\frac{\mathrm{d}\overline{\Phi}_i}{\mathrm{d}t} + \frac{1}{\Delta x_i}(\hat{\mathbf{f}}_{i+1/2} - \hat{\mathbf{f}}_{i-1/2}) = 0, \tag{2.9}$$

where $\hat{\mathbf{f}}_{i+1/2}$ is the numerical flux associated with $x_i + \Delta x_{i+1}/2$, where $x_i \in \overline{\Gamma}$ and $\overline{\Delta x}_i := (\Delta x_{i+1} + \Delta x_i)/2$.

To guarantee flux upwinding, we apply a Lax–Friedrichs flux splitting to each component of the exact flux function: $\mathbf{f}(\Phi) = \mathbf{f}^+(\Phi) + \mathbf{f}^-(\Phi)$ for $\Phi \in \mathscr{E}_{\phi_{\max}}$, where $\mathbf{f}^{\pm}(\Phi) := \frac{1}{2}(\mathbf{f}(\Phi) \pm \alpha\Phi)$ for $\Phi \in \mathscr{E}_{\phi_{\max}}$. The parameter α should equal the spectral radius of $\mathscr{J}_{\mathbf{f}}(\Phi)$. However, a closed formula for this quantity is at least difficult to obtain. For the multi-species traffic model, Zhang et al. [51] choose instead

$$\alpha = \max_{i \in \overline{\Gamma}} \max_{j=1,\ldots,N} \left|v_j(\overline{\Phi}_i)\right|. \tag{2.10}$$

We have adopted this expression and find that it works well for the models studied herein. Nevertheless, recent analyses in [5,51] imply that rigorous estimates of the eigenvalues of $\mathscr{J}_{\mathbf{f}}(\Phi)$, which are available for specific models, are slightly larger, see Sections 3.1 and 3.2.

Note that α is determined anew in each time step. Consequently, the value of Δt is also corrected in each time step respecting the condition $\alpha\Delta t/\overline{\Delta x}_i \leqslant \mathrm{CFL}$, where CFL is the CFL number.

The numerical flux is obtained as sum of the WENO approximations for each flux splitting components:

$$\hat{\mathbf{f}}_{i+1/2} = \mathbf{f}_{i+1/2}^{+,\mathrm{WENO}} + \mathbf{f}_{i+1/2}^{-,\mathrm{WENO}}. \tag{2.11}$$

In Fig. 1 the arrow with "+" corresponds to the approximation $\mathbf{f}^{-,\mathrm{WENO}}$, while the one marked with "−" corresponds to $\mathbf{f}^{+,\mathrm{WENO}}$.

The general WENO scheme is described in a simplified formulation, namely for uniform grids, in [50]. To adapt this simple formulation to the SPR, we follow Holmström's concept [24] to evaluate the differential operator on the sparse representation. Here, the numerical fluxes are computed from data of the same refinement level (local scale) such that all points involved in the computation of one WENO flux vector have the same distance $d_i = \min\{\Delta x_i, \Delta x_{i+1}\}$. If any point is missing, we interpolate the corresponding solution value
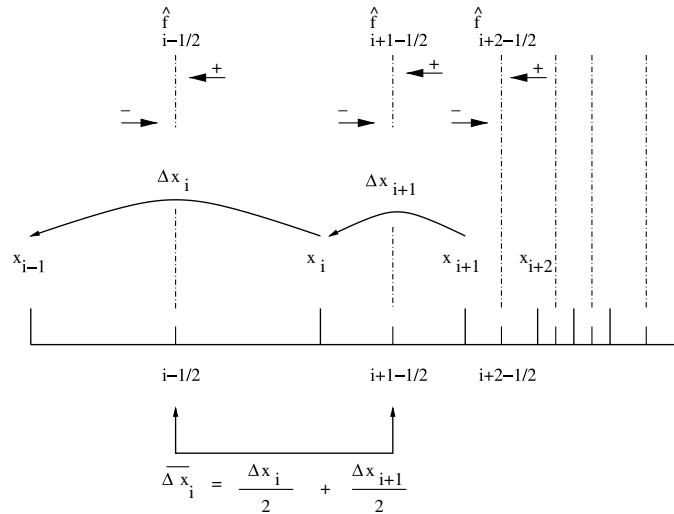
Fig. 1. Positions associated to the SPR, x_i, and staggered positions $x_{i+1/2}$, where the WENO flux is calculated. For each of the N components of the flux vector, a separate WENO approximation is calculated.

from a coarser scale and obtain the necessary flux components. (This procedure is well defined, since all values from the coarsest grid always belong to the SPR.) Values obtained by interpolation are only auxiliary values to keep the stencil locally uniform. No numerical flux will be computed in their positions. Once all numerical flux vectors (2.11) have been computed, the system of ODEs (2.9) could be solved over one time step by an explicit Euler-type method; however, since we herein use a third-order Runge–Kutta method, three rounds of WENO flux computations are necessary to advance the solution over one time step.

The fifth-order WENO approximation takes a convex combination of all possible approximations constructed with three-point stencils, $\mathcal{S}_q = \{x_{i-q}, \ldots, x_{i-q+2}\}$, $q = 0, 1, 2$, which contain the position $x_{i+1/2}$ as an interior point or the nearest neighbor from the boundaries. This point does not belong to the sparse grid $\overline{\Gamma}$. It is just an auxiliary position to calculate the numerical flux. The WENO approximations are computed exactly as is described in the literature, see e.g. [40, Chapter 2]; details are omitted here.

Due to the conservativity of the method in conjunction with the discretization of the zero-flux or periodic boundary conditions, it is ensured that the total mass of each species is conserved.

2.6. Multiresolution algorithm

We present the multiresolution scheme as an operation on the sparse grid $\overline{\Gamma}$, in which numerical fluxes are computed by the above-described WENO procedure. We calculate the approximate solutions $\overline{\Phi}^{n,0}$, $n = 1, 2, \ldots$, until the final time T is reached, by the following algorithm.

Algorithm 2.3

$t \leftarrow 0$
while $t \leqslant T$ **do**

1. $\Phi^n(x)$ is given on the finest grid ($n = 0$) or on a sparse grid ($n > 0$). Use Algorithms 2.1 ($n = 0$) or 2.2 ($n > 0$) to calculate its SPR associated to $\overline{\Gamma}$ with $N_s + 1$ points.
2. Compute the local scale for each point of $\overline{\Gamma}$ and if necessary, the auxiliary neighbors to compute the numerical fluxes with locally uniform stencils.
3. Compute α by (2.10) and $\Delta t \leftarrow \text{CFL} \overline{\Delta x_i}/\alpha$, considering the smallest scale present on $\overline{\Gamma}$ and respecting the CFL condition. Set $t \leftarrow t + \Delta t$.

4. $\overline{\Phi}_j^{(0)} \leftarrow \Phi_j^{n,0}, \ x_j \in \overline{\Gamma}$

do $i = 1, \ldots, n_{RK}$
   (at this point, the values $\overline{\Phi}_j^{(0)}, \ldots, \overline{\Phi}_j^{(i-1)}$ for $x_j \in \overline{\Gamma}$ are known)
   do $k = 0, \ldots, i - 1$

$$\overline{\mathscr{L}}_0(\overline{\Phi}^{(k)}) \leftarrow -\frac{1}{\Delta x_0}\hat{\mathbf{f}}_{1/2}^0, \quad \overline{\mathscr{L}}_{N_s}(\overline{\Phi}^{(k)}) \leftarrow \frac{1}{\Delta x_{N_s}}\hat{\mathbf{f}}_{N_s-1/2}^0$$

$$\overline{\mathscr{L}}_j(\overline{\Phi}^{(k)}) \leftarrow -\frac{1}{\Delta x_j}(\hat{\mathbf{f}}_{j+1/2}^0 - \hat{\mathbf{f}}_{j-1/2}^0), \quad x_j \in \overline{\Gamma} \setminus \{x_0, x_{N_s}\}$$

   enddo

$$\overline{\Phi}_j^{(i)} \leftarrow \sum_{k=0}^{i-1}(\alpha_{ik}\overline{\Phi}_j^{(k)} + \Delta t \beta_{ik}\overline{\mathscr{L}}_j(\overline{\Phi}^{(k)})), \quad x_j \in \overline{\Gamma}$$

enddo
   $\overline{\Phi}_j^{n+1,0} \leftarrow \overline{\Phi}_j^{(n_{RK})}, \quad x_j \in \overline{\Gamma},$
   $n \leftarrow n + 1$
endwhile

2.7. Other boundary conditions

Periodic boundary conditions do not require separate formulas for $\overline{\mathscr{L}}_0$ and $\overline{\mathscr{L}}_{N_0}$, since $\overline{\mathscr{L}}_j$ can always be computed from the "interior" formula if we identify $\overline{\Phi}_{N_s+m}$ with $\overline{\Phi}_m$, $m = 1, 2, 3, \ldots$, according with $\overline{\Gamma}$. Moreover, no extrapolation is needed to compute the WENO interpolation and the filters for the Lagrangian interpolation are always for the centered stencil, as indicated in (2.1). For our examples of initial value problems, however, the computational domain has been chosen large enough so that the solution never reaches its boundary, so Algorithm 2.3 effectively also handles initial value problems.

3. Examples of kinematic flow models

3.1. Traffic flow models

The classic LWR kinematic model [30,35] for unidirectional traffic flow on a single-lane highway starts from the principle of "conservation of cars" $\partial_t\phi + \partial_x(\phi v) = 0$ for $x \in \mathbb{R}$ and $t > 0$, where ϕ is the density of cars as a function of distance x and time t, and v is the velocity of the car located at (x, t). The original LWR model is a single-species model, whose basic assumption $v = v(\phi)$ states that each driver instantaneously adjusts his velocity to the local car density. A common choice is $v(\phi) = v_{\max}V(\phi)$, where $v_{\max}$ is a maximum velocity a driver assumes on a free road, and the hindrance function $V(\phi)$ models the presence of other cars, which urges each driver to adjust his speed. Thus, the flux is

$$f(\phi) := \phi v(\phi) = \begin{cases} v_{\max}\phi V(\phi) & \text{for } 0 \leqslant \phi \leqslant \phi_{\max}, \\ 0 & \text{otherwise}, \end{cases} \tag{3.1}$$

where $\phi_{\max}$ is the maximum "bumper-to-bumper" car density. The simplest obvious choice is the linear interpolation $V(\phi) = V_1(\phi) := 1 - \phi/\phi_{\max}$.

Recently, Wong and Wong [46] and Benzoni-Gavage and Colombo [2] independently formulated an extension of the LWR model to multi-class traffic flow, considering that cars belong to a finite number N of classes (species), each associated with a function $v = v_i(\Phi)$. It is assumed that drivers of each species adjust their velocity to the global car density $\phi = \phi_1 + \cdots + \phi_N$ seen at a point (x, t), which implies $v_i(\Phi(x,t)) = v_i(\phi(x,t))$ for $i = 1, \ldots, N$, and that all drivers adjust their velocity in the same way, such that

$$v_i(\Phi) = v_{max}^i V(\phi), \quad i = 1, \ldots, N. \tag{3.2}$$

Here, v_{max}^i is the maximum velocity attained by car species i and the function $V : [0, \phi_{max}] \rightarrow [0, 1]$ describes the attitude of drivers [2], that is, represents the same hindrance function as in the single-class case.

For the traffic model, we may assume a circular road of length L and assume an initial traffic density

$$\Phi(x, 0) = \Phi^0(x) = (\phi_1^0(x), \ldots, \phi_N^0(x))^{\mathrm{T}} \in \mathscr{E}, \quad 0 \leqslant x \leqslant L. \tag{3.3}$$

The periodicity condition is

$$\phi_i(0, t) = \phi_i(L, t), \quad t > 0, \ i = 1, \ldots, N; \tag{3.4}$$

however, we herein only consider compactly supported data and relatively short simulation times, so that our solutions are also solutions to the initial value problem posed for $x \in \mathbb{R}$, that is, for an infinite road.

Finally, a recent analysis by Zhang et al. [51] implies that for $0 < v_{max}^1 < v_{max}^2 < \cdots < v_{max}^N$, the eigenvalues $\lambda_i = \lambda_i(\Phi)$, $i = 1, \ldots, N$, of the Jacobian $\mathscr{J}_{\mathbf{f}}(\Phi)$ of (1.4) satisfy

$$v_1 + V'(\phi)(\phi_1 v_{max}^1 + \cdots + \phi_N v_{max}^N) \leqslant \lambda_1 \leqslant v_1 \leqslant \lambda_2 \leqslant \cdots \leqslant v_{N-1} \leqslant \lambda_N \leqslant v_N \quad \forall \Phi \in \mathscr{E}_{\phi_{max}},$$

where $v_i = v_i(\Phi)$, $i = 1, \ldots, N$. Since the leftmost expression is bounded, but possibly negative for sufficiently large ϕ, and using (3.2), an estimate α of the spectral radius $\varrho(\mathscr{J}_{\mathbf{f}}(\Phi))$ with $\alpha \leqslant \varrho(\mathscr{J}_{\mathbf{f}}(\Phi))$ is given by

$$\alpha = \max \left\{ v_{max}^N V(\phi), |v_{max}^1 V(\phi) + V'(\phi)(\phi_1 v_{max}^1 + \cdots + \phi_N v_{max}^N)| \right\}.$$

3.2. Sedimentation of polydisperse suspensions

We consider a polydisperse suspension of rigid spherical particles which are dispersed in a viscous fluid of density ϱ_{f} and of dynamic viscosity μ_{f}. The solid particles belong to N different species having size (diameter) d_i and density ϱ_i, $i = 1, \ldots, N$, where $d_i \neq d_j$ or $\varrho_i \neq \varrho_j$ for $i \neq j$, and $d_1 \geqslant d_2 \geqslant \cdots \geqslant d_N$. Model equations for the three-dimensional motion of the mixture were derived in [11] from the mass and linear momentum balances for the fluid and each solid species, introducing constitutive assumptions and simplifying the model equations as a consequence of a dimensional analysis. Details are presented in [5,10,11] and are omitted here. The relevant parameters are $\delta_i := d_i^2/d_1^2$ and $\bar{\varrho}_i := \varrho_i - \varrho_{\mathrm{f}}$ for $i = 1, \ldots, N$. Here, ϕ_{max} denotes a maximum solids volume fraction, which we here assume to be constant. Moreover, we introduce the vector $\bar{\varrho} := (\bar{\varrho}_1, \ldots, \bar{\varrho}_N)^{\mathrm{T}}$, the cumulative solids fraction $\phi := \phi_1 + \cdots + \phi_N$, the viscosity parameter $\mu := -g d_1^2/(18\mu_{\mathrm{f}}) < 0$, where g is the acceleration of gravity and the hindered settling factor $V = V(\phi)$, which may be chosen as

$$V(\phi) = \begin{cases} (1 - \phi)^{n-2} & \text{if } \Phi \in \mathscr{E}_{\phi_{max}} \\ 0 & \text{otherwise,} \end{cases} \quad n > 2. \tag{3.5}$$

Then, according to the MLB model, the phase velocity of particle species i is given by

$$v_i(\Phi) = \mu V(\phi) \left[\delta_i(\bar{\varrho}_i - \bar{\varrho}^{\mathrm{T}}\Phi) - \sum_{m=1}^{N} \delta_m \phi_m(\bar{\varrho}_m - \bar{\varrho}^{\mathrm{T}}\Phi) \right], \quad i = 1, \ldots, N. \tag{3.6}$$

For one-dimensional batch settling of a suspension with initially given composition in a closed vessel of depth L, the initial condition is again (3.3), while the zero-flux boundary conditions are

$$\mathbf{f}|_{x=0} = \mathbf{f}|_{x=L} = 0. \tag{3.7}$$

When the particles differ in size only (i.e., $\varrho_1 = \varrho_2 = \cdots = \varrho_N =: \varrho_{\mathrm{s}}$ and $d_1 > d_2 > \cdots > d_N$), (3.6) simplifies to the following expression, where $v_\infty = \mu(\varrho_{\mathrm{s}} - \varrho_{\mathrm{f}})$ is the Stokes velocity, that is, the settling velocity of a single particle in an unbounded medium, of the largest species:

$$v_i(\Phi) = v_\infty(1 - \phi)V(\phi)(\delta_i - (\delta_1\phi_1 + \cdots + \delta_N\phi_N)), \quad i = 1, \ldots, N. \tag{3.8}$$

Choices of $v_1(\Phi), \ldots, v_N(\Phi)$ for the polydisperse sedimentation model alternative to (3.6) are discussed in [9,48].

The ellipticity criterion for $N = 2$ is equivalent to a criterion [1] for the occurrence of instabilities like blobs and fingering in bidisperse sedimentation [45]. By a perturbation analysis, it was shown in [11] that loss of hyperbolicity, that is the occurrence of complex eigenvalues of $\mathscr{J}_{\mathbf{f}}(\Phi)$, provides an instability criterion for polydisperse suspensions of *arbitrary* numbers of species N. In [5,11] it is shown that the MLB model has desirable stability properties. In [5] it is proved that for equal-density particles ($\bar{\varrho}_1 = \cdots = \bar{\varrho}_N = \varrho_s - \varrho_f$), *arbitrary N* and particle size distributions, the system (1.5) is strictly hyperbolic for all $\Phi \in \mathscr{E}$ with $\phi_1 > 0, \ldots, \phi_N > 0$ and $\phi < 1$ if the flux vector (3.6) is chosen. The proof is similar to that of Rosso and Sona [36] outlined in Section 1.2. The hyperbolicity, and thus stability result for equal-density spheres is in agreement with experimental evidence since instability phenomena never have been observed with this type of mixtures, but always involve particles of different specific densities [45].

For the equal-density case, Berres et al. [5] show that the eigenvalues $\lambda_i = \lambda_i(\Phi)$, $i = 1, \ldots, N$, of $\mathscr{J}_{\mathbf{f}}(\Phi)$ satisfy

$$\forall \Phi \in \mathscr{E}_{\phi_{\max}}: \quad v_1(\Phi) \leqslant \lambda_1 \leqslant v_2(\Phi) \leqslant \cdots \leqslant v_N(\Phi) \leqslant \lambda_N \leqslant \varphi(\Phi),$$
$$\varphi(\Phi) := \mu(\varrho_s - \varrho_f)(-2\boldsymbol{\delta}^{\mathrm{T}}\Phi V(\phi)(1 - \phi) + (V(\phi)(1 - \phi))'(\boldsymbol{\delta}^{\mathrm{T}}\Phi + \phi)), \tag{3.9}$$

where $\boldsymbol{\delta} := (\delta_1, \ldots, \delta_N)^{\mathrm{T}}$. Since $v_i(\Phi) \leqslant 0$ for $i = 1, \ldots, N$, but possibly $\varphi(\Phi) > 0$ for ϕ sufficiently large, a rigorous estimate α of the spectral radius $\varrho(\mathscr{J}_{\mathbf{f}}(\Phi))$ with $\alpha \leqslant \varrho(\mathscr{J}_{\mathbf{f}}(\Phi))$ is given by $\alpha = \max\{|v_1(\Phi)|, \varphi(\Phi)\}$. It is worth noting that if the function $V(\phi)$ is given by (3.5), for example, and $\Phi \in \mathscr{E}_{1/n} \subset \mathscr{E}_{\phi_{\max}}$, then $\varphi(\Phi)$ does not exceed the velocity of the interstitial fluid (see [11] for details), so that at least in the dilute regime, all eigenvalues are bounded by the velocities of the N solids phases or the fluid phase. Note that (3.9) is not valid for suspensions with particles having different densities.

3.3. Separation of oil-in-water dispersions

Rosso and Sona [36] analyze the separation of small oil droplets in an oil-in-water dispersion. The model outlined in [36] can be written in the form (1.2) if we consider oil droplets of N volumes $\mathscr{V}_1 > \mathscr{V}_2 > \cdots > \mathscr{V}_N > 0$, where x is the upward-increasing height variable and $\phi_i = \phi_i(x,t)$ is the volume fraction occupied by droplets of volume $\mathscr{V}_i$. As Rosso and Sona [36] argue, the differential motion of the particle species is not driven by differences in viscosity. The basic nonlinearity is introduced by a viscosity function $\mu_d = \mu_d(\Phi)$. If we denote again by μ_f the viscosity of pure water (without oil), then $\mu_d(\Phi)$ is assumed to satisfy $\mu_d \in C^1(\mathscr{E})$, $\mu_d(\Phi) > 0$ and $\partial\mu_d/\partial\phi_i > 0$ for $i = 1, \ldots, N$ for all $\Phi \in \mathscr{E}_{\phi_{\max}}$ and $\mu_d(0, \ldots, 0) = \mu_f$. The velocity functions $v_1(\Phi), \ldots, v_N(\Phi)$ are then given by

$$v_i(\Phi) = c\frac{\mathscr{V}_i^{2/3}}{\mu_d(\Phi)}(1 - \phi), \quad i = 1, \ldots, N, \quad c := \frac{2g(\varrho_f - \varrho_{\text{oil}})}{9(4\pi/3)^{2/3}},$$

where g, ϱ_f and ϱ_{oil} denote the acceleration of gravity, the density of pure water and density of pure oil, respectively. For separation of a dispersion in a column of height L, we could again employ the initial and boundary conditions (3.3) and (3.7).

4. Numerical examples

4.1. Multi-species traffic model (Examples 1 and 2)

In [49] Zhang et al. present numerical simulations of a traffic flow model with $N = 9$ species (classes) of vehicles with the maximum velocities $v_{\max}^i = (52.5 + i \cdot 7.5)$ km/h, $i = 1, \ldots, 9$. We consider here Cases 1 and 2 simulated in [49], where the function $V(\phi) = \exp(-(\phi/\phi_*)^2/2)$ with the parameter $\phi_* = 50$ cars/km is used. Both cases, which form our Examples 1 and 2, consist of the evolution of an isolated initial traffic 'platoon' given by

$$\Phi^0(x) = p(x)\phi^0(0.04, 0.08, 0.12, 0.16, 0.2, 0.16, 0.12, 0.08, 0.04)^{\mathrm{T}},$$
$$p(x) := \begin{cases} 10x & \text{for } 0 < x \leqslant 0.1, \quad -10(x - 1) & \text{for } 0.9 < x \leqslant 1, \\ 1 & \text{for } 0.1 < x \leqslant 0.9, \quad 0 & \text{otherwise,} \end{cases} \tag{4.1}$$

where x denotes distance measured in kilometers, and $\phi^0 = 40$ cars/km in Case 1 of [49] (our Example 1) and $\phi^0 = 120$ cars/km in Case 2 of [49] (our Example 2).

For the numerical simulations of Examples 1 and 2, the coarsest and finest grids of the multiresolution representation consist of 2^4 and $N_0 = 2^{15}$ points, respectively, where the total number of points of a scale refers to
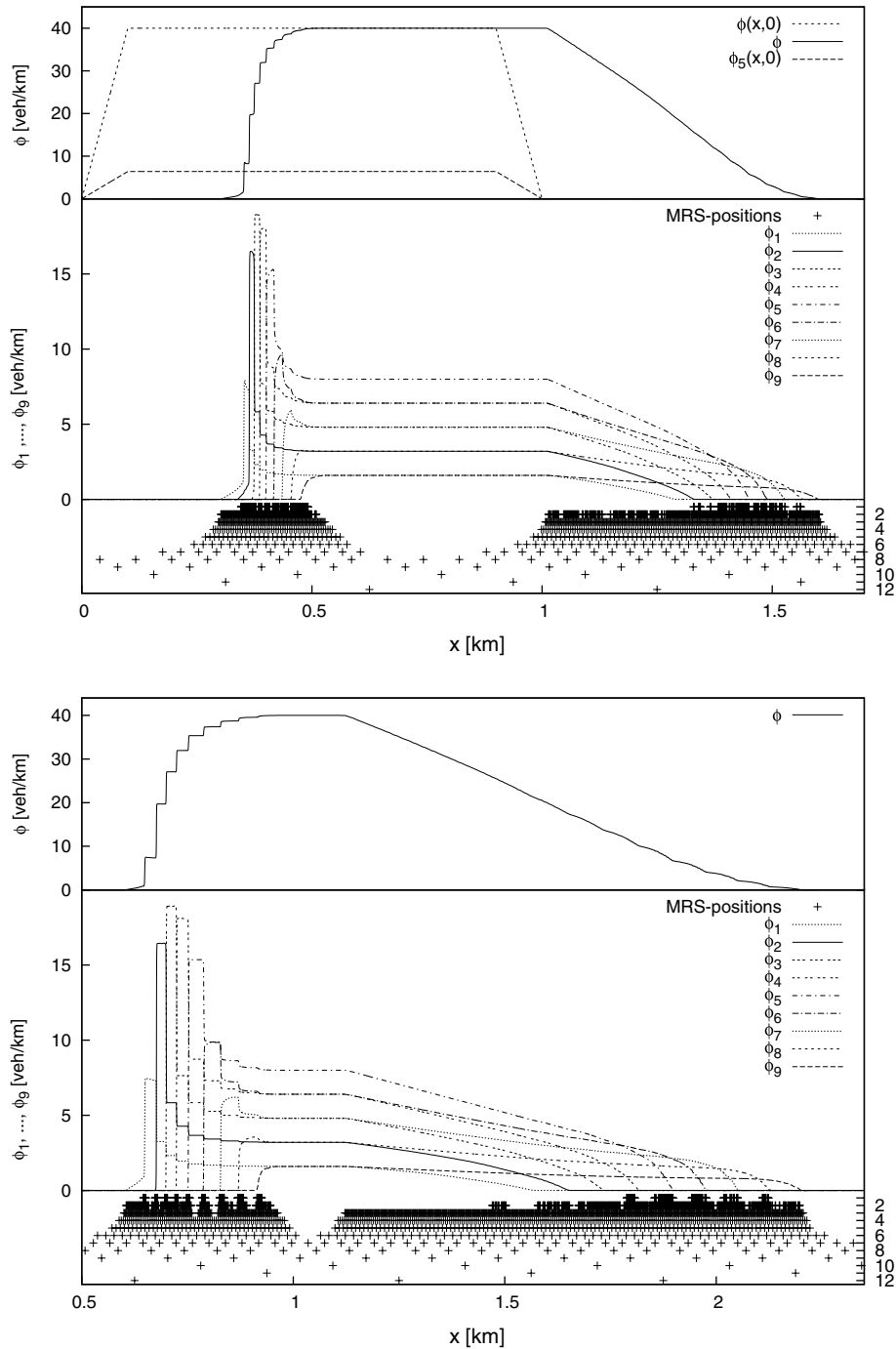

Fig. 2. Example 1 (traffic model, $N = 9$): numerical solution at $t = 0.005$ h (top) and $t = 0.01$ h (bottom). The top plot also shows the initial data $\phi_5(x,0)$ and $\phi(x,0)$. Here and in Figs. 3, 8 and 9, the numbers $2, 4, \ldots, 12$ of the right vertical axis represent the level k of the multiresolution. The finest grid, $k = 0$, is represented by the numerical solution.

the x-interval $[0, 10\,\text{km}]$. The threshold values are $\varepsilon_0 = 10^{-3}$, $\varepsilon_k = 2.5\varepsilon_{k-1}$ and $\theta_k = 2.5\varepsilon_k$, $k = 1, \ldots, L_c$ and CFL $= 0.15$ for both cases. Here and in Examples 3–6, the interpolator used in the interpolating multiresolution transform is the one given by (2.1) with $r = 4$ or its non-periodic version (2.2).

Figs. 2 and 3 show portraits of the numerical solution of Example 1 at four different times, along with corresponding positions of significant multiresolution coefficients. Fig. 4 shows the evolution of the number of significant multiresolution coefficients, or equivalently, of the compression rate. The left diagram of Fig. 5 displays the total simulated density ϕ at six different times, while the right diagram shows simulated traffic
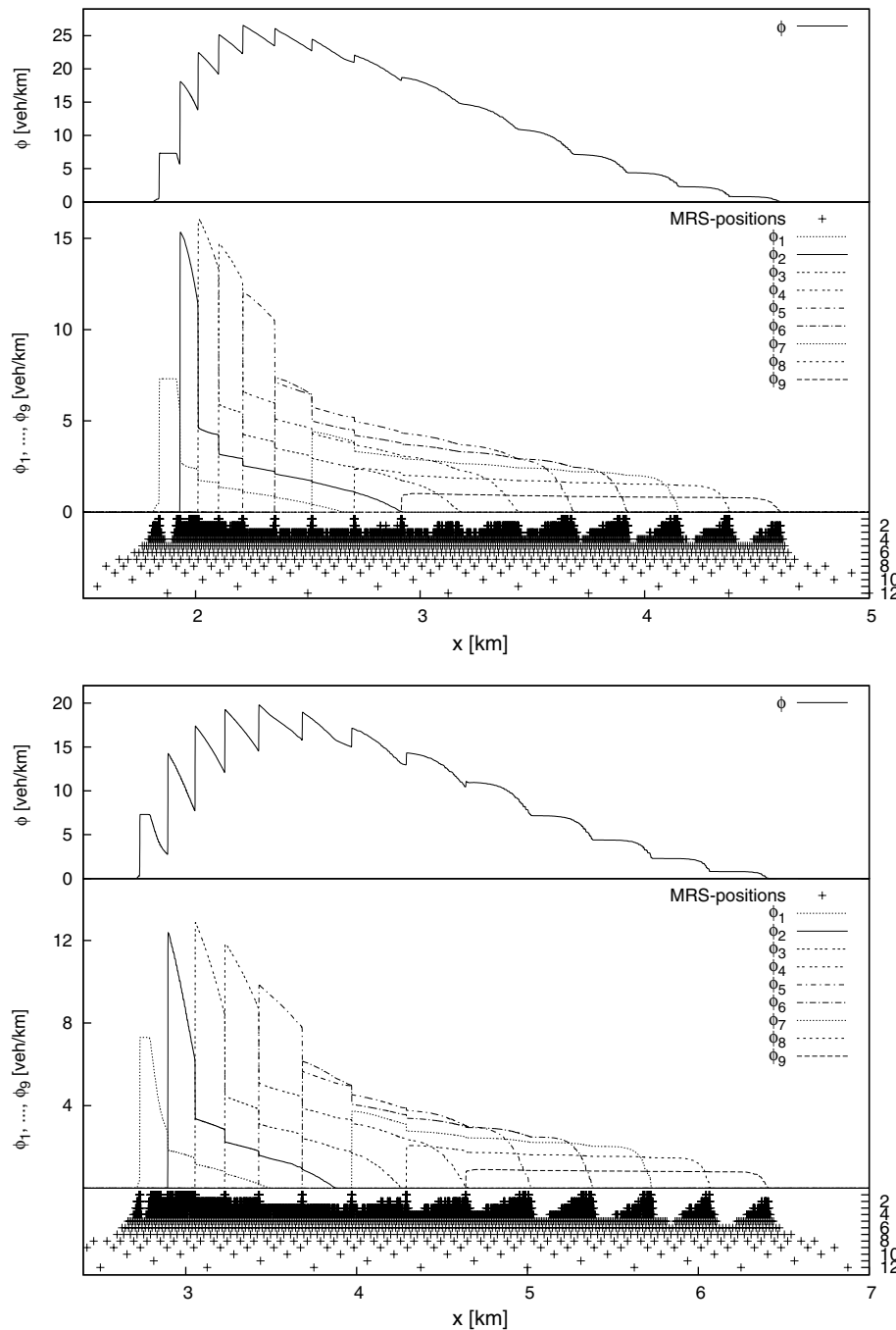
Fig. 3. Example 1 (traffic model, $N = 9$): numerical solution at $t = 0.03$ h (top) and $t = 0.045$ h (bottom).
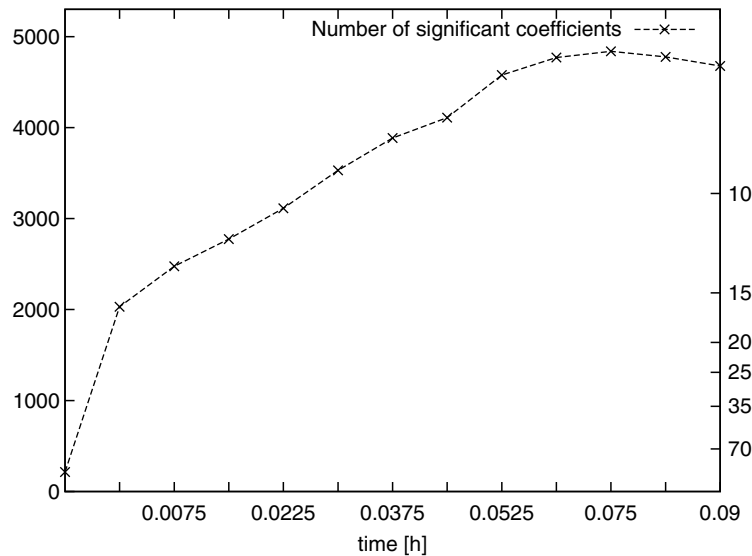
Fig. 4. Example 1 (traffic model, $N = 9$): number of significant wavelet coefficients per iteration. The corresponding compression rates are indicated on the right vertical axis.
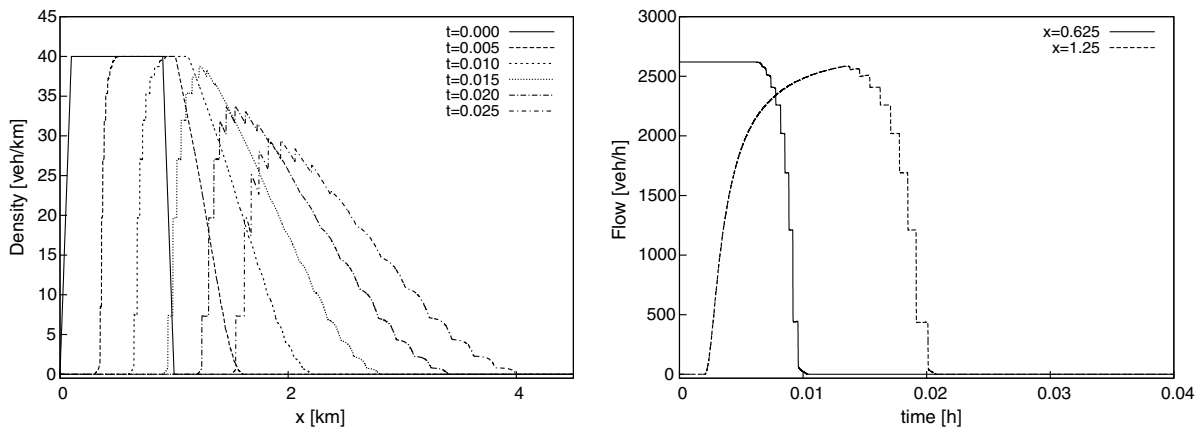
Fig. 5. Example 1 (traffic model, $N = 9$): simulation of total density ϕ at different times (left) and traffic flow as a function of time at $x = 0.625$ km and $x = 1.25$ km (right).

flow at two different spatial positions as functions of time. Figs. 6 and 7 compare numerical results at one fixed time obtained by the WENO-MRS method for $N_0 = 2^{13}$, 2^{14} and 2^{15} points in the finest grid with a solution obtained from the WENO method on a fixed mesh with 2^{13} points, i.e., with $\Delta x = 10$ km/$8192 = 1.221 \times 10^{-3}$ km. We restrict ourselves to short x-intervals displaying the solution component ϕ_4 and the cumulative density ϕ in the left and right plots of Fig. 6, respectively.

Figs. 2 and 3 show how the WENO-MRS method adaptively concentrates computational effort in regions of strong variation, that is, near the shocks that separate regions of different composition. These shocks are resolved very sharply, as are thin layers between them. Moreover, the multiresolution method moves with the solution: the finer levels are used on the support of the solution (that is, where the density is different from zero) only. In the initial stage of the simulation, as can be seen in the top plot of Fig. 2, for example, the solution is composed of kinematic shocks and smooth density variations at both ends of what initially was a platoon, and that both zones are separated by a short segment where all components are constant and only the three coarsest levels are occupied. On the other hand, the plots of Fig. 3 show that the transition of the concentration profiles of each species to zero value at the right end of their support takes place continuously, but
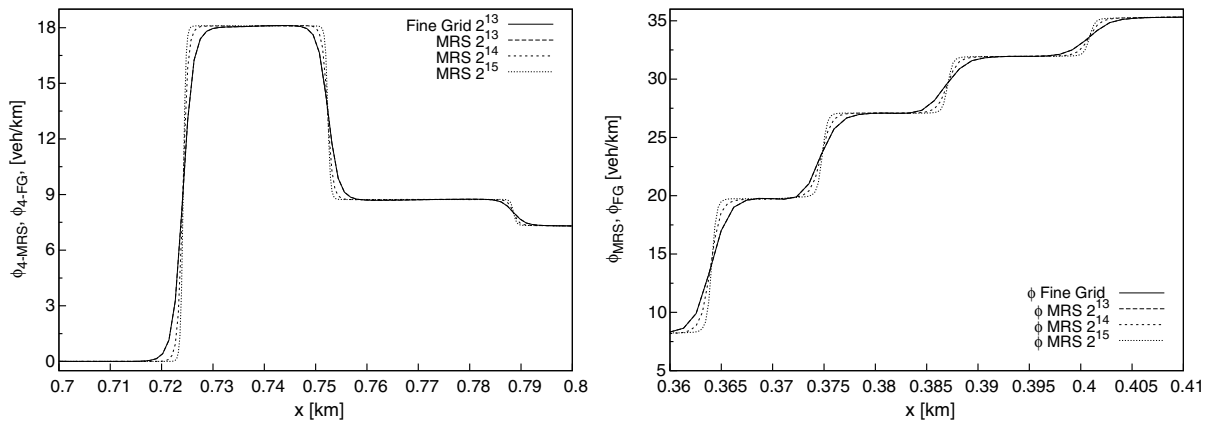
Fig. 6. Example 1 (traffic model, $N = 9$): comparison between a uniform fine-grid WENO solution with 2^{13} points and the WENO-MRS method with 2^{13}, 2^{14} and 2^{15} points. Left: solution component ϕ_4, right: total density ϕ at $t = 0.01$ h.
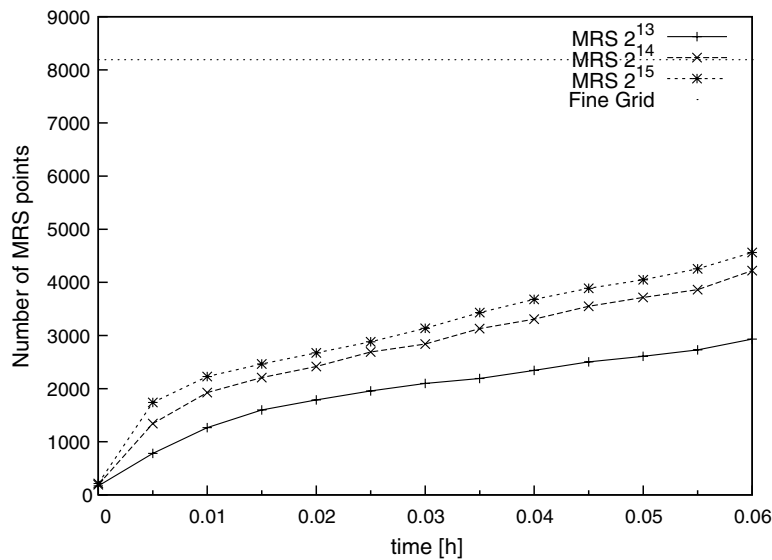

Fig. 7. Example 1 (traffic model, $N = 9$): comparison between a uniform fine-grid WENO solution with 2^{13} points (subdividing the interval $[0, 10]$) and the WENO-MRS method with 2^{13}, 2^{14} and 2^{15} points: number of points used in each case.

not smoothly, such that a "kink" appears. The multiresolution technique handles this situation by developing a sawtooth-shaped feature. This feature is visible e.g. between $x = 4.5$ km and $x = 6.5$ km in the bottom plot of Fig. 3, where the grid to the left of each "kink" is slowly coarsened as the derivative of the solution of each component slowly increases (with x decreasing) to zero value. The number of points used in our multiresolution method for this case is always less than 5000 (see Fig. 4), such that the compression rate achieved is always better than six.

Examples 1 and 2 have been chosen such that comparison with the numerical results obtained by Zhang et al. [49], who used fixed-grid WENO schemes, is possible. The accuracy used in [49] is 1600 grid points for the x-interval $[0, 2$ km$]$, which is roughly equivalent to 2^{13} points on the x-interval $[0, 10]$.

Fig. 5 presents the same solution as Fig. 6 of [49]. However, in [49] solutions are becoming slightly oscillatory, for example, as is visible in the left plot of Fig. 6 of [49] in the $t = 0.025$ h profile between $x = 1.5$ km and $x = 1.6$ km, or in the right plot of the same figure in the $x = 1.2$ km flux plot near $t = 0.02$ h, whereas our profiles are not oscillatory in corresponding positions, see Fig. 5. Note that the $t = 0.015$ h profile included in

the left plot of Fig. 5 permits comparison with the solutions shown in Fig. 5 of [49], where the performance of the Lax–Friedrichs and WENO schemes at various discretizations are compared.

Furthermore, Fig. 6 on one hand illustrates that the uniform grid WENO solution is almost identical to the WENO-MRS solution obtained on the same underlying (finest) grid (with 2^{13} points); on the other hand, we see that the resolution becomes sharper when we pass to WENO-MRS solutions with 2^{14} or 2^{15} grid points.
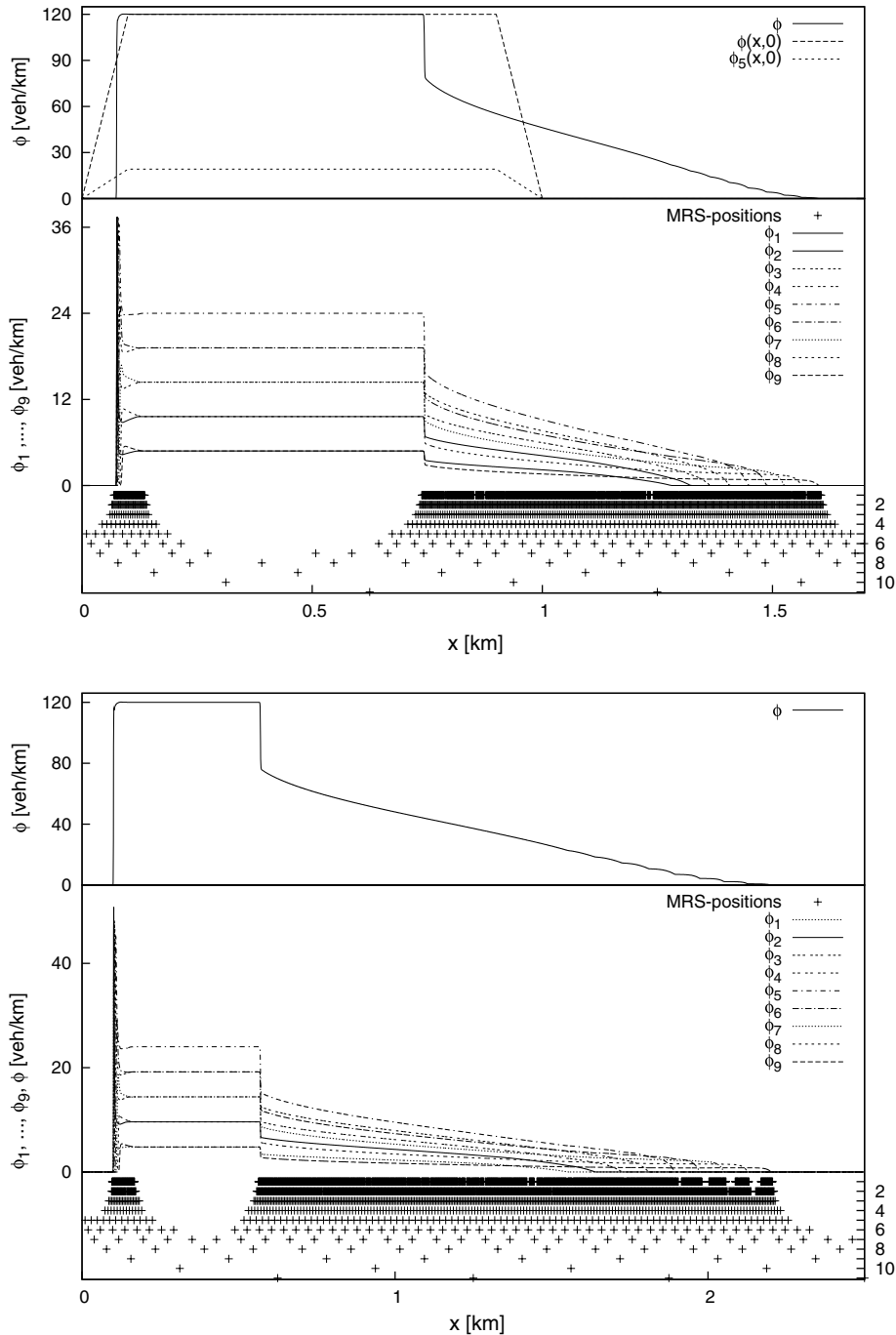
Fig. 8. Example 2 (traffic model, $N = 9$): numerical solution at $t = 0.005$ h (top) and $t = 0.01$ h (bottom). The top plot also shows the initial data $\phi_5(x,0)$ and $\phi(x,0)$.

The increase of accuracy under refinement is unsurprising, but note that for this example, according to Fig. 7, the number of significant positions of the 2^{14} grid is less than twice that of the 2^{13} grid and that the 2^{15} grid involves only slightly more significant positions than the 2^{14} grid, so the increase of accuracy is achieved under moderate increase of computational effort only. Fig. 7 also illustrates that the number of significant positions of all WENO-MRS solutions shown in Figs. 2, 3, 5 and 6 always remains below the number 2^{13} associated with the fixed grid.
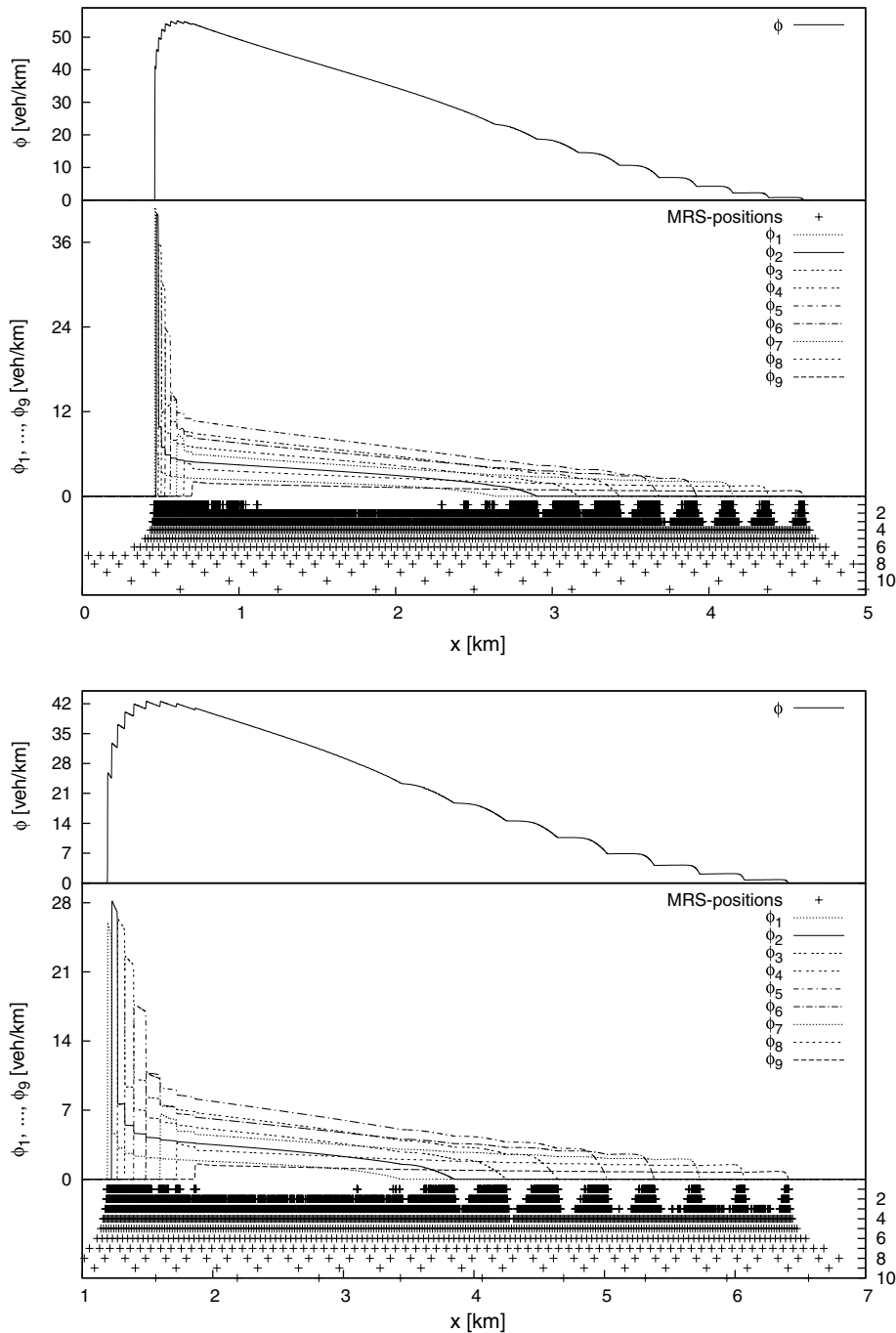
Fig. 9. Example 2 (traffic model, $N = 9$): numerical solution at $t = 0.03$ h (top) and $t = 0.045$ h (bottom).

The preceding observations are in general also valid for Example 2. For that case, Figs. 8 and 9 show the numerical solution at four different times, along with corresponding positions of significant multiresolution coefficients. Fig. 10 shows the evolution of the number of significant multiresolution coefficients, or equivalently, of the compression rate attained. The left diagram of Fig. 11 displays the total simulated density ϕ at seven different times, while the right diagram shows the simulated traffic flow at two different spatial positions as functions of time.

The numerical solution of Example 2 evolves in a slightly different way than that of Example 1, since an appreciable zone is formed in which all solution components decrease smoothly (for example, in the top plot of Fig. 9, this zone is roughly located between $x = 0.8$ km and $x = 2.5$ km). The multiresolution method adapts itself to this continuous variation, since significant positions on the second finest, but not on the finest level are filled. Fig. 10 again illustrates the efficiency of the method, since the number of significant coefficients for our simulation remains well below the number of 2^{15} fine grid positions.
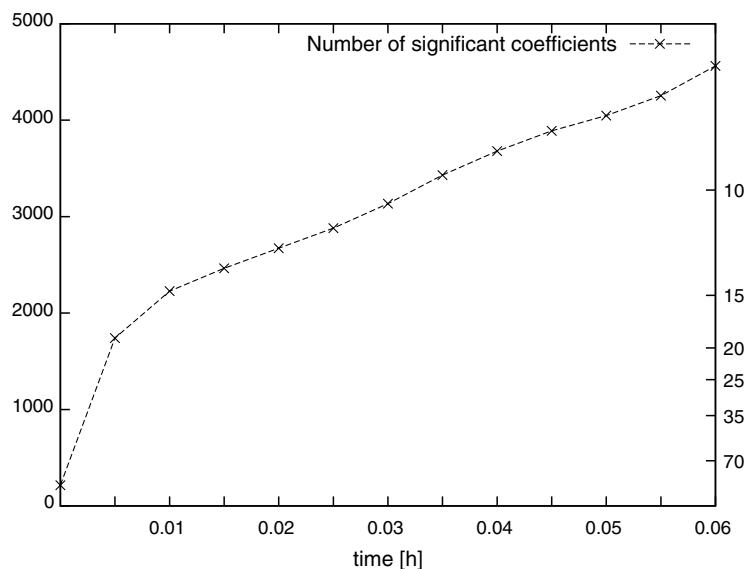
Fig. 10. Example 2 (traffic model, $N = 9$): number of significant wavelet coefficients per iteration, with compression rates indicated on the right vertical axis.
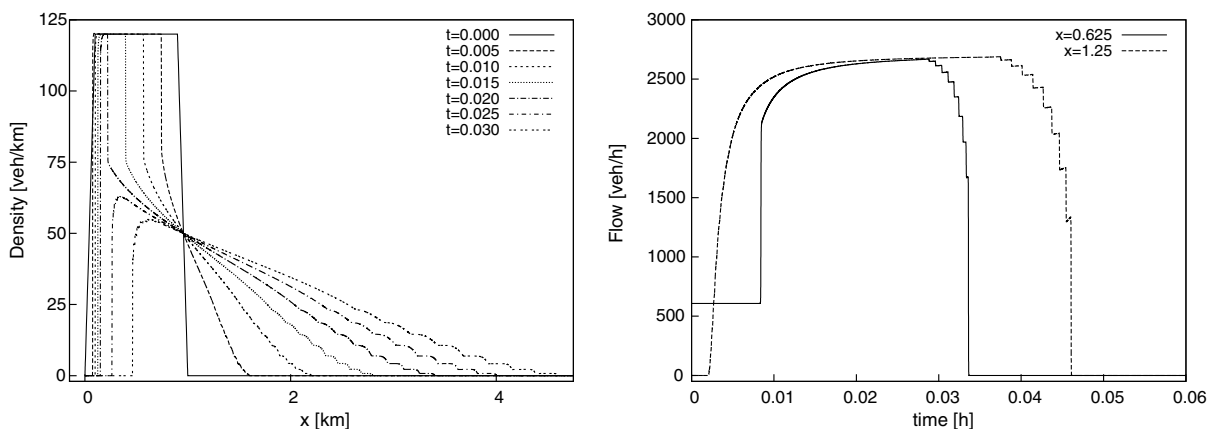
Fig. 11. Example 2 (traffic model, $N = 9$): simulation of total density ϕ at different times (left) and traffic flow as a function of time at $x = 0.625$ km and $x = 1.25$ km (right).

The parameters of our Example 2 are the same as that of Case 2 in [49]. The solution profiles of both diagrams of Fig. 11 can be compared with numerical results displayed in Fig. 10 of [49], which again were obtained by a fifth-order WENO scheme on a uniform fine grid with $\Delta x = 2$ km/1600.

4.2. Sedimentation of polydisperse suspensions (Examples 3–6)

4.2.1. Settling of a bidisperse suspension of equal-density spheres (Example 3)

The experiment by Schneider et al. [38] is a standard test case for analytical and numerical techniques for polydisperse suspensions, and is used here for the WENO-MRS method. In this example, the parameters are $N = 2$, $\varrho_1 = \varrho_2 = \varrho_s = 2790$ kg/m^3, $d_1 = 4.96 \times 10^{-4}$ m, $d_2 = 1.25 \times 10^{-4}$ m, $\varrho_f = 1208$ kg/m^3 and $\mu_f = 0.02416$ Pa s. Here, we have $\delta_1 = 1$ and $\delta_2 = d_2^2/d_1^2 = 0.06351213$. For this mixture, we select the phase space $\mathscr{E}_{0.68}$ [10] and the function $V(\phi)$ given by (3.5) with the exponent $n = 4.7$, as suggested in [38]. As in [38], we consider an initially homogeneous suspension with $\Phi^0 = (\phi_1^0, \phi_2^0)^{\mathrm{T}} = (0.2, 0.05)$ in a vessel of height $L = 0.3$ m. In our simulation, the coarsest and finest grids consist of 2^3 and 2^{14} subintervals, respectively. The threshold values are $\varepsilon_0 = 10^{-6}$, $\varepsilon_k = 2.0\varepsilon_{k-1}$ and $\theta_k = 2.0\varepsilon_k$, $k = 1, \ldots, L_c$ and CFL = 0.15.

Fig. 12 shows the numerical solution as concentration profiles at four different times, together with the significant positions of the multiresolution representation. Furthermore, we calculated a local density of significant multiresolution positions by subdividing the interval $[0, L]$ into $2^7 = 128$ subintervals, counting the total number of significant positions in each subinterval, and dividing the result by the maximal possible number of 2^7 significant positions per subinterval. The result has been plotted in the left diagram of Fig. 13. Finally, the
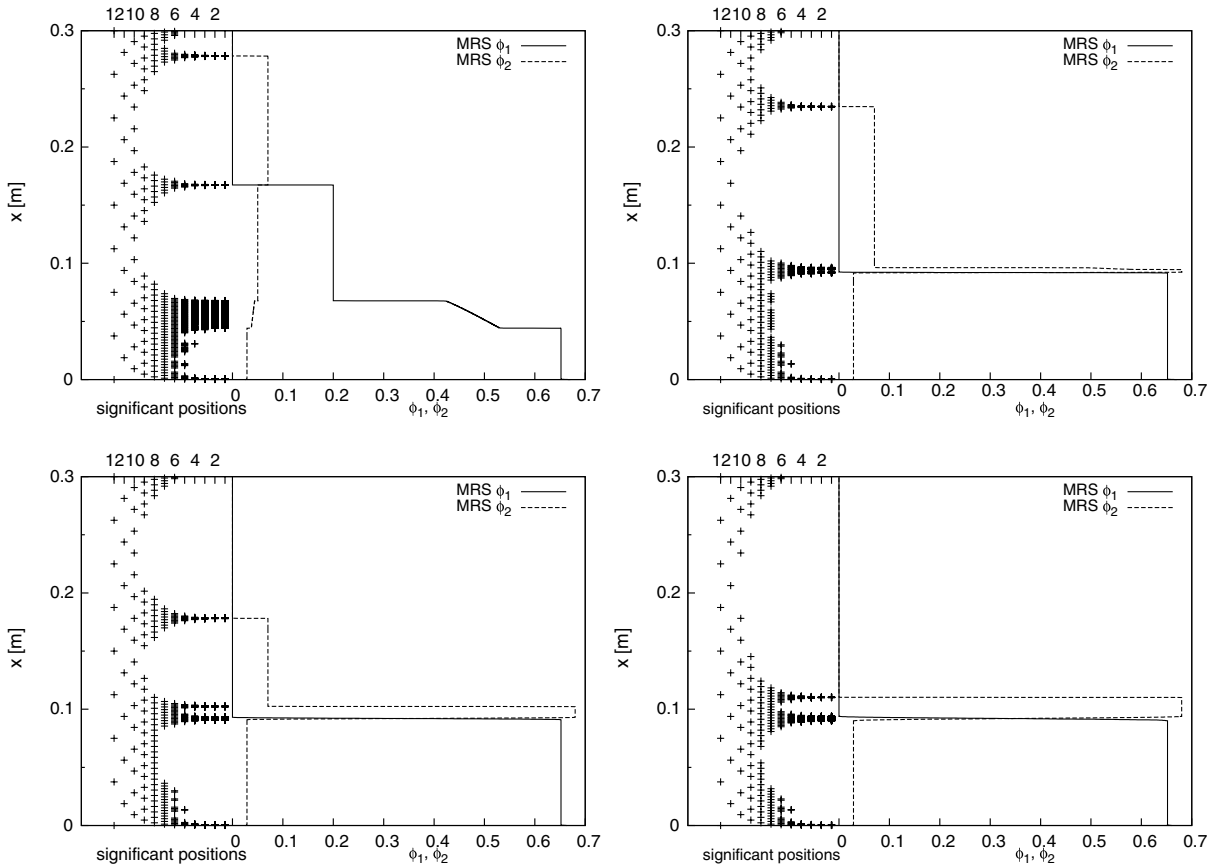

Fig. 12. Example 3 (sedimentation model, $N = 2$): numerical solution at $t = 54$ s (top left), $t = 164$ s (top right), $t = 302$ s (bottom left) and $t = 599.18$ s (bottom right). Here and in Figs. 16, 19, 21, 22 and 23 the numbers $2, 4, \ldots, 10, 12$ of the top horizontal axis represent the level k of the multiresolution. The finest grid, $k = 0$, is represented by the numerical solution.
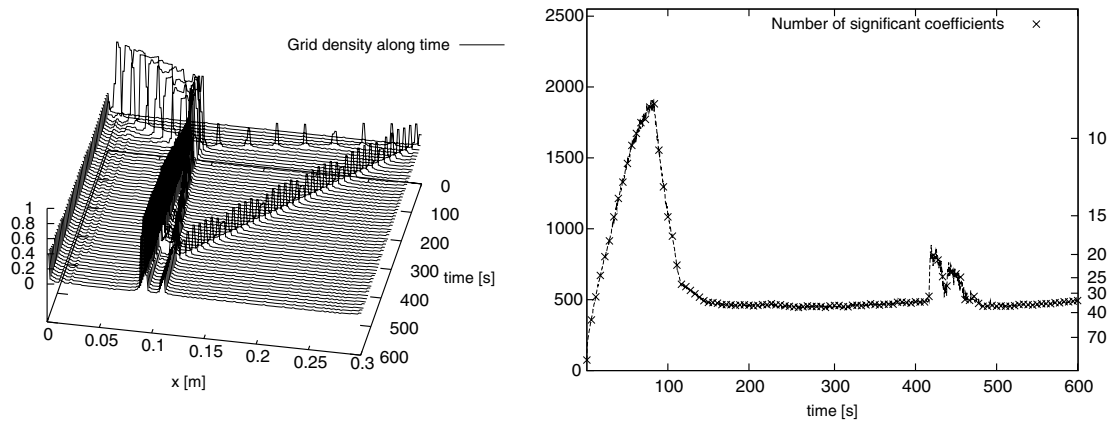
Fig. 13. Example 3 (sedimentation model, $N = 2$): plot of the density of significant wavelet coefficients (left) and number of significant wavelet coefficients per iteration (right). In the right diagram, compression rates are indicated on the right vertical axis.

Table 1
Example 3: Simulation times for MRS solutions, considering different threshold values ε_0 and an initial fine grid with 2^{14} points

ε_0	10^{-2}	10^{-3}	10^{-4}	10^{-5}	10^{-6}	10^{-7}	Uniform grid ($\varepsilon_0 = 0$)
CPU time [min]	269.65	292.80	327.85	401.27	478.69	612.10	1371.66
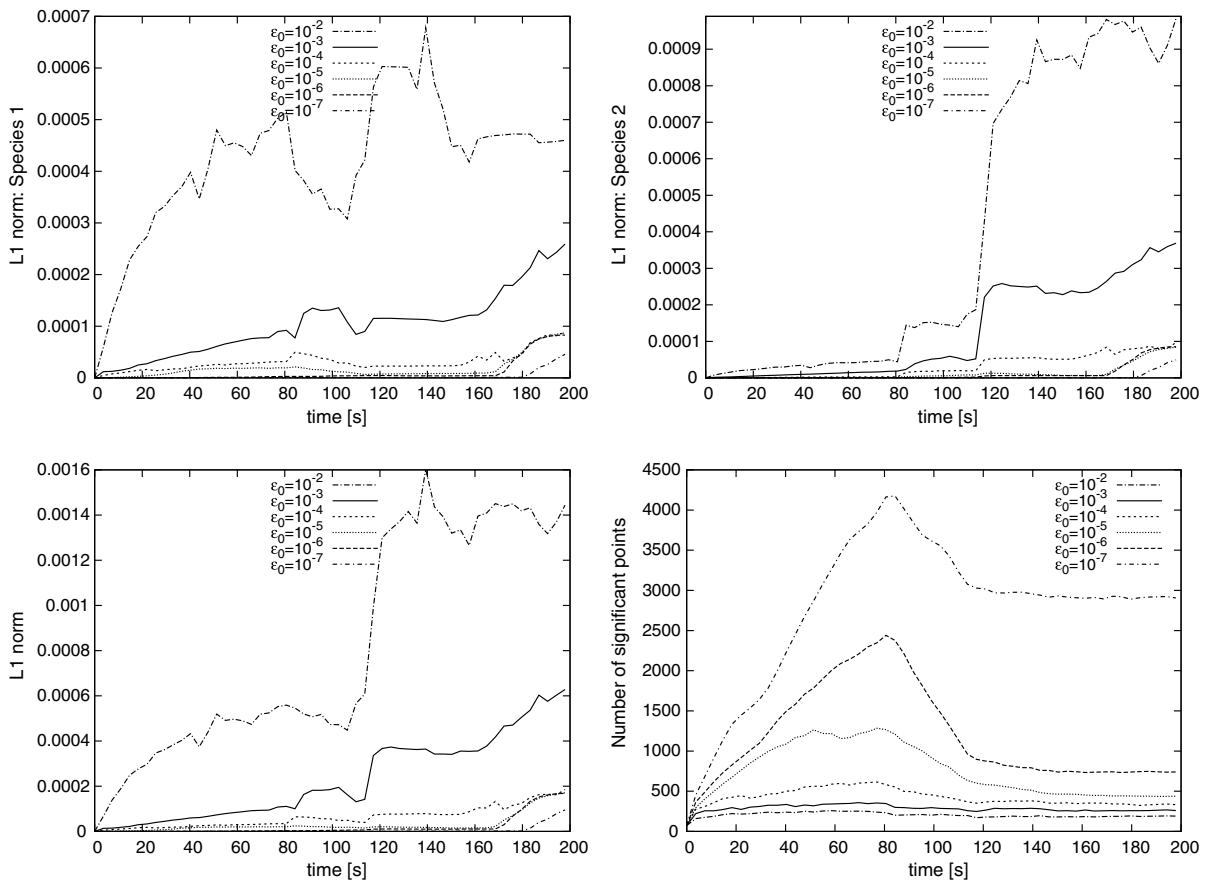
Fig. 14. Example 3: approximate L^1 error for ϕ_1 (top left), ϕ_2 (top right) and ϕ (bottom left) produced by WENO-MRS method with different threshold values ε_0. The bottom right plot shows the number of significant details.

right diagram of Fig. 13 shows the evolution of the total number of significant positions and the equivalent compression rate as a function of time.

The sedimentation model is associated with boundary conditions, and our multiresolution solution displays a concentration of significant positions near the boundaries $x = 0$ and $x = L$. Apparently, the exact solution approximated is the same as the one simulated earlier in [9,10] by the Nessyahu–Tadmor [34] and the Kurganov–Tadmor [27] methods, respectively. A recent semi-analytical solution construction [4] confirms that this
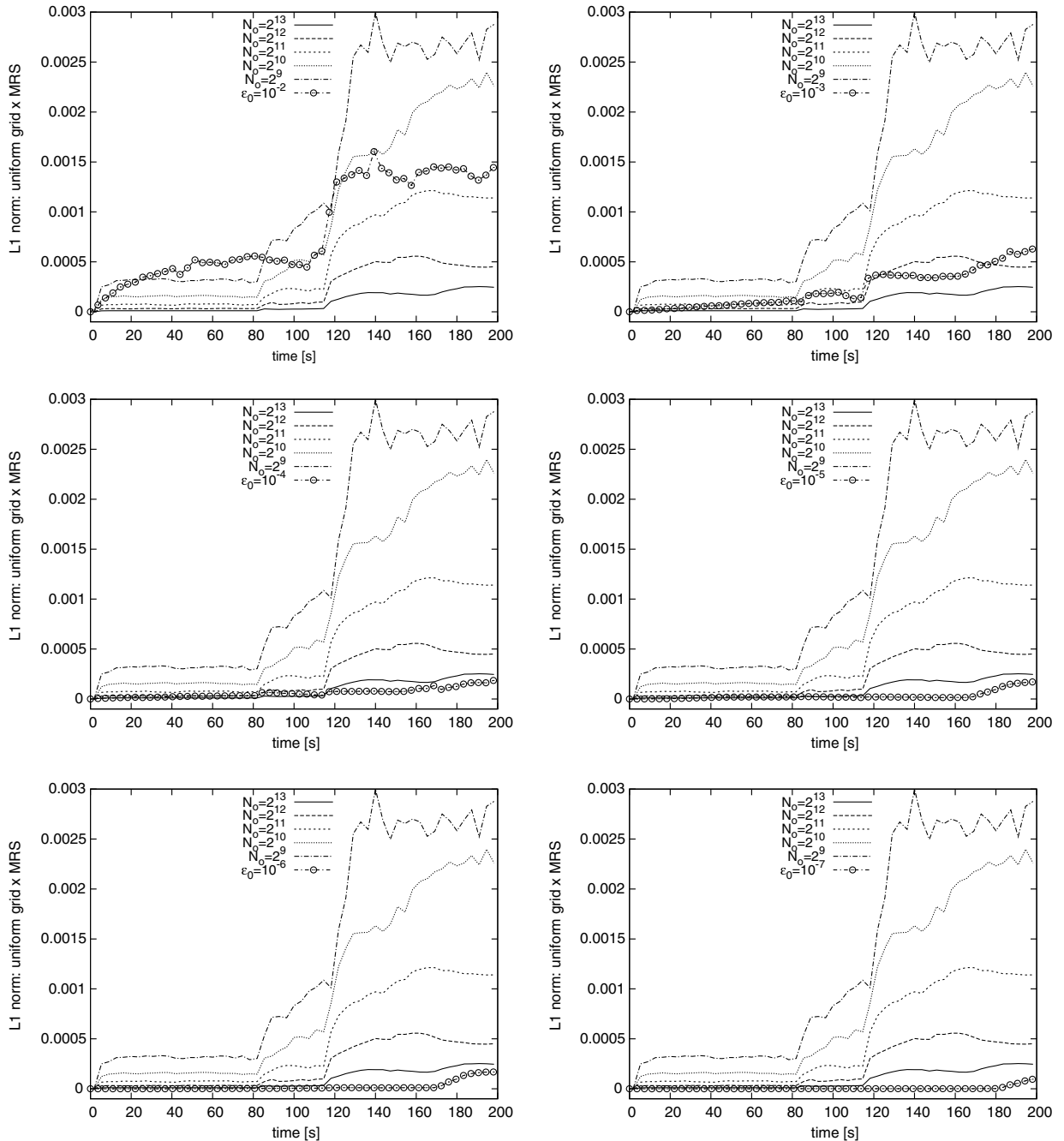
Fig. 15. Example 3: approximate L^1 error in ϕ produced by the WENO-MRS method for six choices of ε_0 compared with errors generated by the WENO scheme on equidistant (non-sparse) grids with N_0 subintervals.

Table 2
Example 3: Simulation times for fine grid solutions, considering different discretizations

N_0	2^9	2^{10}	2^{11}	2^{12}	2^{13}	2^{14}
CPU time [min]	2.03	8.05	31.50	129.51	548.87	1371.66

solution satisfies Liu's entropy condition, which enforces that several kinematic shocks appearing in the original construction advanced in [38] be replaced by continuous transitions (rarefaction waves). Such a rarefaction wave appears in the $t = 54$ s plot (top left) of Fig. 12 near $x = 0.05$ m. Another basic feature of the solution is the formation of a thin layer of sediment, consisting of the smaller species 2 only, on top of a sediment consisting mainly of the larger species 1, with a small fraction of the smaller species 2. Our solution shows that this layer of sediment is accurately reproduced by the WENO-MRS scheme. Overall, the scheme also handles this example efficiently, since except at the boundary, significant positions of the finest grids appear near the kinematic shocks only. This also becomes apparent in the left diagram of Fig. 13. Finally, the right diagram of Fig. 13 shows that for this class of problems, which in many circumstances leads to a final solution consisting of areas of constant composition separated by stationary shocks, the WENO-MRS method allows considerable compression rates.

The threshold value ε_0 and the choice of ε_k for each level k play a special role for the performance of the WENO-MRS method, since computational time and accuracy are related to their variations. For Example 3, Table 1 shows how computational time increases with decreasing values of ε_0, indicating the increase of computational effort incurred by more restrictive thresholding.
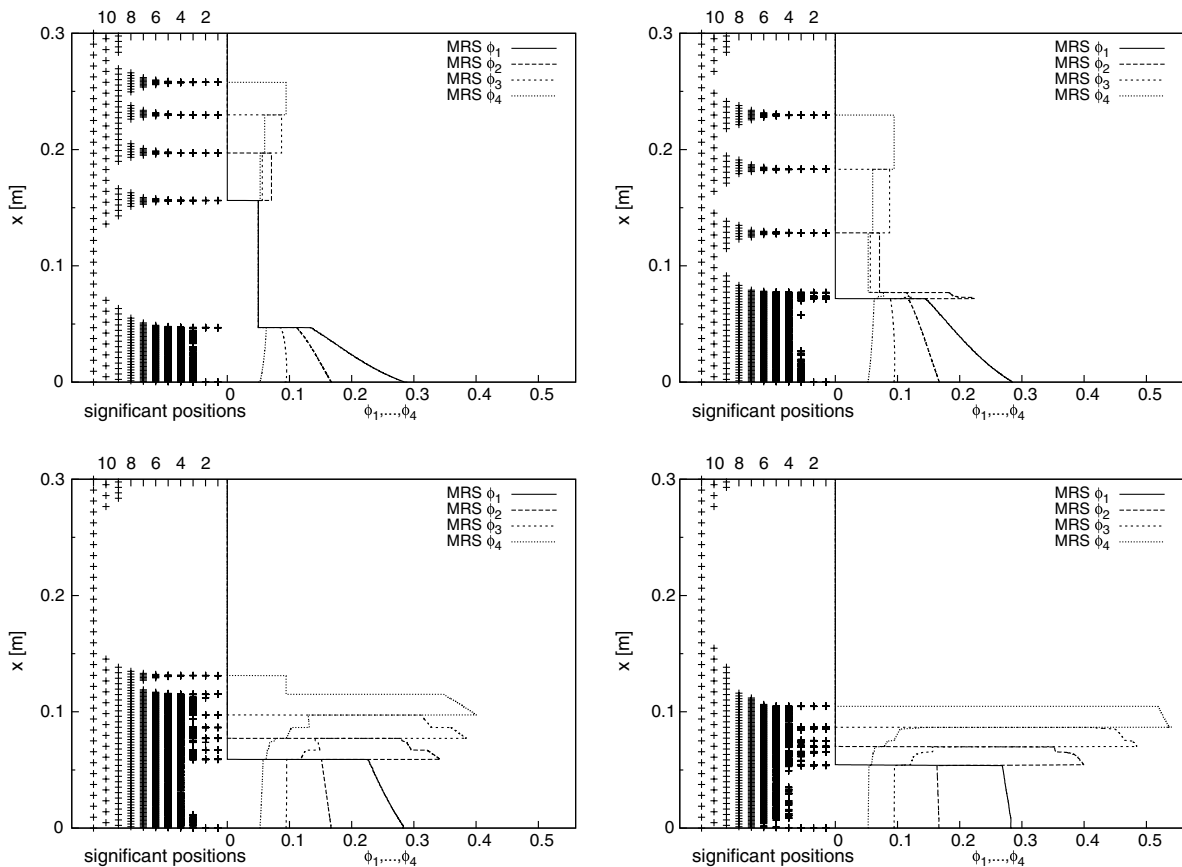

Fig. 16. Example 4 (sedimentation model, $N = 4$): numerical solution at $t = 51.65$ s (top left), $t = 86.08$ s (top right), $t = 106.60$ s (bottom left) and $t = 792.37$ s (bottom right).

On the other hand, we performed two additional numerical experiments based on Example 3 in order to study the effect of different choices of the parameter ε_0. The result of the first of these additional experiments is presented in Fig. 14, which shows the evolution of the approximate error in L^1 norm under different choices of the threshold value ε_0, where the strategy to obtain ε_k is kept as in the previous discussion of this example, $\varepsilon_k = 2.0\varepsilon_{k-1}$. The finest grid in the WENO-MRS method consists of $N_0 = 2^{14}$ subintervals. The error is computed here with respect to a fine-grid reference solution. We observe that the error consistently decreases as the threshold value decreases. It is emphasized that within our WENO-MRS method, the solution is not computed on a uniform grid in order to possibly correct the multiresolution (thresholding) parameters or to decrease the error between different time iterations. The wavelet transform is needed to adaptively generate the SPR of the solution, that is, it controls the grid adaptivity, but a posteriori error estimates are not utilized here.

The second additional numerical experiment is based on the same WENO-MRS solutions whose errors are displayed in Fig. 14, but we are now interested in comparing the performance of the WENO-MRS method in terms of CPU time and accuracy (L^1 error) with solutions obtained on a sequence of equidistant (non-sparse) grids. In Fig. 15 we again display the approximate L^1 error in ϕ generated by various choices of ε_0, each one in a separate plot, and add the corresponding approximate L^1 errors produced by the conventional WENO scheme on equidistant, fine grids with the indicated numbers N_0 of subintervals. The plots of Fig. 15 indicate that for the three choices $\varepsilon_0 = 10^{-5}$, 10^{-6} and 10^{-7}, the error obtained by the WENO-MRS solution is always smaller than, and for $\varepsilon_0 = 10^{-4}$ is for large times ($t > 120$ s) smaller than, the error obtained by a solution on a uniform grid with $N_0 = 2^{13}$. Furthermore, Tables 1 and 2 allow to compare the time spend with the MRS solution and with the uniform solution with 2^{13} points. Of course there exists an "overhead" associated with the WENO-MRS method, since generating and updating a solution point belonging to an SPR is considerably more costly than handling one such point in a uniform grid.

In this work, we do not measure specifically the time required for running through each block of routines, and due to the diversity and nonlinearity of the models, a reliable uniform estimate of the percentage of effort that goes into the administration of the multiresolution representation seems difficult. We do, however, acknowledge that this "overhead" is still considerable for the example chosen. For example, Table 1 tells us that our WENO-MRS method with ε_0 speeds up the computation (compared with a solution on the underlying uniform fine grid) by a factor of 2.86. On the other hand, the right plot of Fig. 13 implies that during the
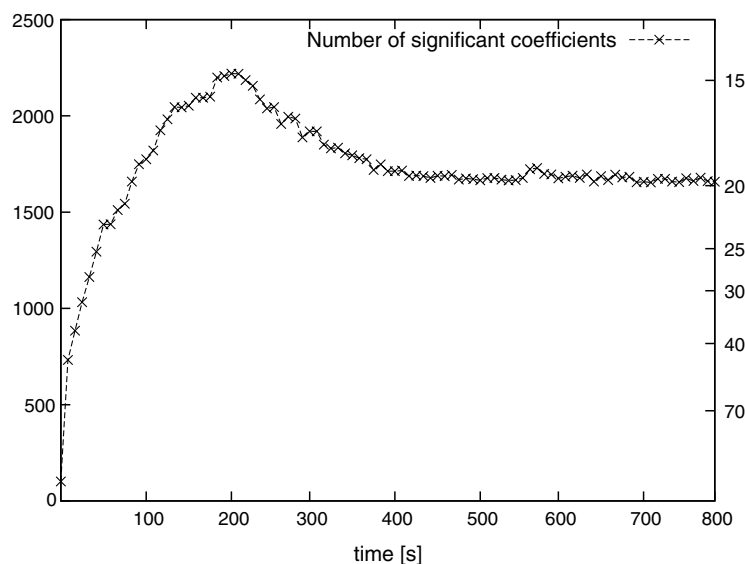

Fig. 17. Example 4 (sedimentation model, $N = 4$): number of significant wavelet coefficients per iteration, with compression rates indicated on the right vertical axis.

time interval [0,200 s], the SPR never contains more than 2^{11} points. The computation time for a solution on a *uniform* grid with $N_0 = 2^{11}$ points without multiresolution is, however, only 31.5 min.

This example (as do others presented herein) shows that for the class of models considered, the number of wavelet coefficients can vary strongly with respect of the choice of the threshold value ε_0. The choice of this threshold value forms a heuristic component, which is a limitation to be surmounted. Furthermore, since the MRS "overhead" is significant, it would be interesting to attempt speeding up the present method by keeping the SPR unaltered over several time steps. Of course, our WENO-MRS method could be improved significantly if the limitation of the time step according to the finest grid size were removed, as in the recent finite volume multiresolution schemes by Stiriba and Müller [42]. In any case, the sharp concentration of significant positions near the shocks forming in this and other examples, and the adaptive buildup of the SPR display that the gain of memory is satisfactory.

4.2.2. Settling of a suspension with particles of four different sizes (Example 4)

This example is related to work by Greenspan and Ungarish [21] and Bürger et al. [9], who consider the settling of a 4-disperse suspension ($N = 4$) of particles having the same density but different sizes, corresponding to $\delta_2 = 0.64$, $\delta_3 = 0.36$ and $\delta_4 = 0.16$. The solution construction for this case is presented in [21] in dimensionless terms. As in [9], we here adopt the same (nominal) parameters as for Example 3 ($\varrho_s = 2790$ kg/m³, $d_1 = 4.96 \times 10^{-4}$ m, $\varrho_f = 1208$ kg/m³, $\mu_f = 0.02416$ Pa s, $L = 0.3$ m) so that results are comparable. In accordance with [21], the hindered settling factor is chosen as the following variant of (3.5):

$$V(\phi) = \begin{cases} (1 - \phi/\phi_{\max})^{n-2} & \text{if } \Phi \in \mathscr{E}_{\phi_{\max}} \\ 0 & \text{otherwise,} \end{cases} \quad n > 2; \tag{4.2}$$

here, we choose $\phi_{\max} = 0.6$, $n = 4$, and as in [9], $\Phi^0 = (0.05, 0.05, 0.05, 0.05)^{\mathrm{T}}$.

For this case, the coarsest and finest grids consist of 2^5 and 2^{15} points, respectively. The threshold values are $\varepsilon_0 = 10^{-5}$, $\varepsilon_k = 2.5\varepsilon_{k-1}$ and $\theta_k = 2.5\varepsilon_k$, $k = 1, \ldots, L_c$ and CFL = 0.1 for both cases.

Fig. 16 shows the numerical solution at four different times, along with the corresponding significant positions, while Fig. 17 records the number of significant coefficients or the equivalent compression rate.

The top two plots of Fig. 16 illustrate that the significant positions of the multiresolution method accurately move with the four downwards-propagating shocks. These shocks include three sectors in which, from top to bottom, only species 4, species 3 and 4 and species 2, 3 and 4 are present. Note that in these three zones, the predicted concentrations of the present species is higher than the initial concentration 0.05. This effect is
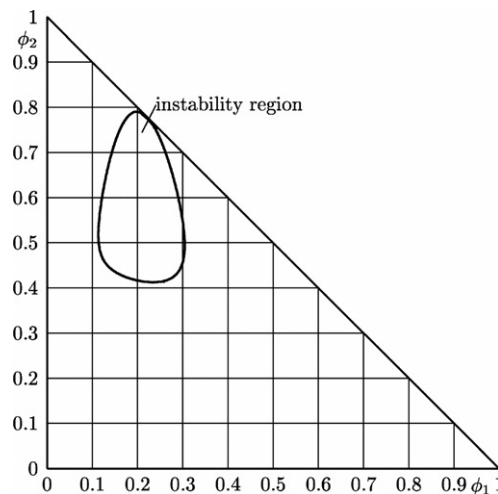

Fig. 18. Example 5 (sedimentation model, $N = 2$): instability region of the MLB model for $\delta_2 = d_2^2/d_1^2 = 0.044112$, $\bar{\varrho}_1 = 500$ kg/m³ and $\bar{\varrho}_2 = 1450$ kg/m³.

consistent with the Rankine–Hugoniot condition (1.6), is also predicted by the shock construction done in [21], and is observed experimentally [41].

For $N = 1$, using (4.2) with $n = 4$ produces a solution that will never attain a steady state. This is basically due to the horizontal tangent the function $\phi \mapsto \phi V(\phi)$ has at the end $\phi = \phi_{max}$ of its support, and therefore admits arbitrarily slow rarefaction waves. In other words, due to our choice of (4.2), we cannot expect that a steady state appears within finite time, as is the case in Example 3. Rather, we have to deal with slowly moving shocks. This has become apparent in Figs. 14–16 of [9]. As the bottom right plot of our Fig. 16 shows, the multiresolution method is well adapted to handle this situation, since the three finest grids are occupied near the kinematic shocks only. Moreover, our Fig. 17 indicates that the total number of significant positions remains nearly constant in the nearly stationary situation, so that refinement and thresholding are well balanced, as one should expect for slowly moving zones of strong variation.

4.2.3. Settling of a bidisperse suspension of particles having two different densities (Example 5)

We consider a bidisperse suspension ($N = 2$) studied experimentally by Moritomi et al. [33]. The suspension consists of particles of two different sizes and densities with $\delta_2 = d_2^2/d_1^2 = 0.044112$, $\bar{\varrho}_1 = 500$ kg/m^3 and $\bar{\varrho}_2 = 1450$ kg/m^3. The viscosity parameter is $\mu = -3.2819 \times 10^{-4}$ m^4/(kg s). Note that particles of the smaller species 2 have a larger density. For this mixture, we set $\phi_{max} = 0.68$ and use (3.5) with $n = 4.7$. We consider the settling of an initially homogeneous suspension of composition $\Phi^0 = (0.04, 0.04)^{\mathrm{T}}$ in a vessel of height $L = 1$ m. It should be emphasized that this example is anomalous in that the model equations have an appreciable instability (ellipticity) region, see Fig. 18.
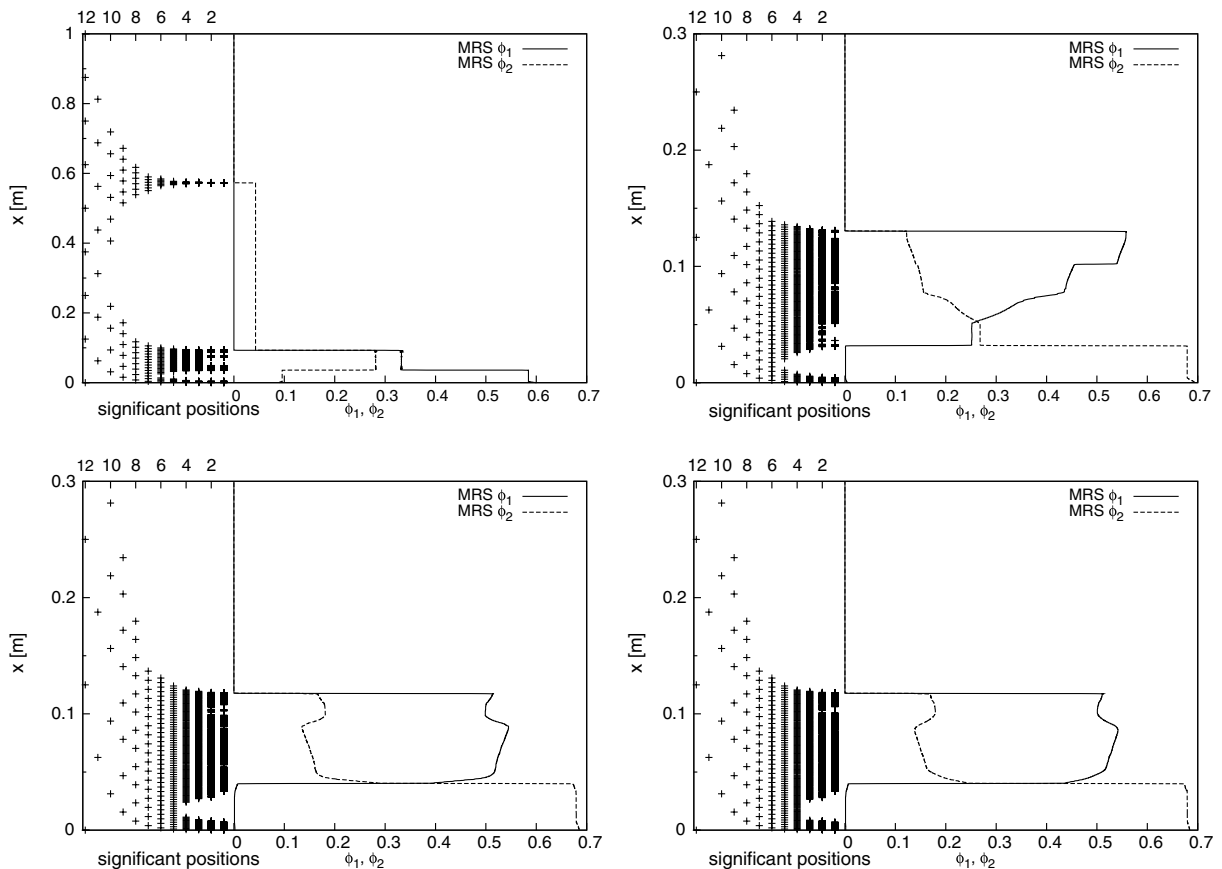

Fig. 19. Example 5 (sedimentation model, $N = 2$): simulation of the settling of a suspension of particles having different densities and sizes at $t = 25$ s (top left), $t = 75$ s (top right), $t = 225$ s (bottom left) and $t = 350$ s (bottom right).

For this example, the coarsest and finest grids consist of 2^3 and 2^{14} points, respectively. The threshold values are $\varepsilon_0 = 10^{-6}$, $\varepsilon_k = 2.0\varepsilon_{k-1}$ and $\theta_k = 2.0\varepsilon_k$, $k = 1, \ldots, L_c$ and CFL = 0.1 for both cases.

Fig. 19 shows the solution together with the set of significant positions and Fig. 20 shows the evolution of the number of significant positions. In this example, the WENO-MRS method again produces a good approximation with due refinement of the zones of strong variation. As is shown in [4], for the selected initial datum the solution construction, which obeys Liu's entropy condition, avoids the ellipticity region, i.e. only values from the hyperbolicity (stability) region are assumed. Moreover, as is also shown in [4], a stationary solution develops that includes continuous variations (with respect to x) of the sediment composition, and does not only consist of different layers of constant composition separated by stationary kinematic shocks. Actually, a necessary condition for these continuous variations to occur is that the particles have different densities [4]. We observe that the WENO-MRS solution reproduces this behaviour, and yields a solution similar to Figs. 4(a) and 4(b) of [6].
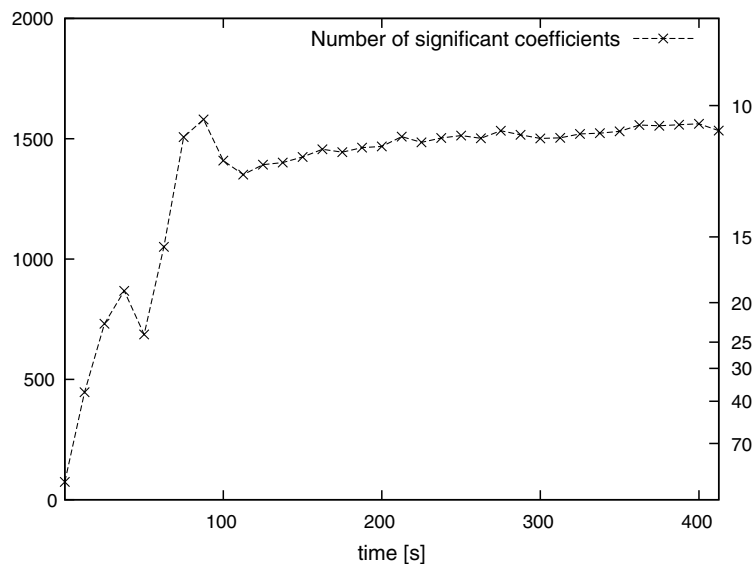

Fig. 20. Example 5 (sedimentation model, $N = 2$): number of significant wavelet coefficients per iteration, with compression rates indicated on the right vertical axis.

Table 3
Parameters for the settling of a suspension with $N = 11$ particle sizes

i	d_i [10^{-5} m]	δ_i	ϕ_i^0
1	8.769	1.0000	0.000435
2	8.345	0.9056	0.003747
3	7.921	0.8159	0.014420
4	7.497	0.7309	0.032603
5	7.073	0.6506	0.047912
6	6.649	0.5749	0.047762
7	6.225	0.5039	0.032663
8	5.801	0.4376	0.015104
9	5.377	0.3760	0.004511
10	4.953	0.3190	0.000783
11	4.529	0.2668	0.000060

4.2.4. Settling of a suspension with particles of 11 different sizes (Example 6)

To illustrate that the multiresolution technique is suited to handle systems with a large number of particle species, we consider a suspension of equal-density particles of $N = 11$ different sizes. The parameters and initial concentrations of these size classes are displayed in Table 3. This size distribution was determined by Tory et al. [44] as a discrete approximation for a suspension of closely-sized spherical particles with continuously, roughly normally distributed particle sizes [39]. Following [39], we consider a settling column of height $L = 0.935$ m. The hindered settling factor found suitable is (3.5) with $n = 4.65$ and $\phi_{max} = 0.641$. According to [39], a single sphere with diameter 6.694×10^{-5} m has a Stokes velocity of $\tilde{v}_\infty = -0.00392$ m/s, so we here use (3.8) with $v_\infty = (8.769/6.694)^2 \tilde{v}_\infty = -0.00673$ m/s.
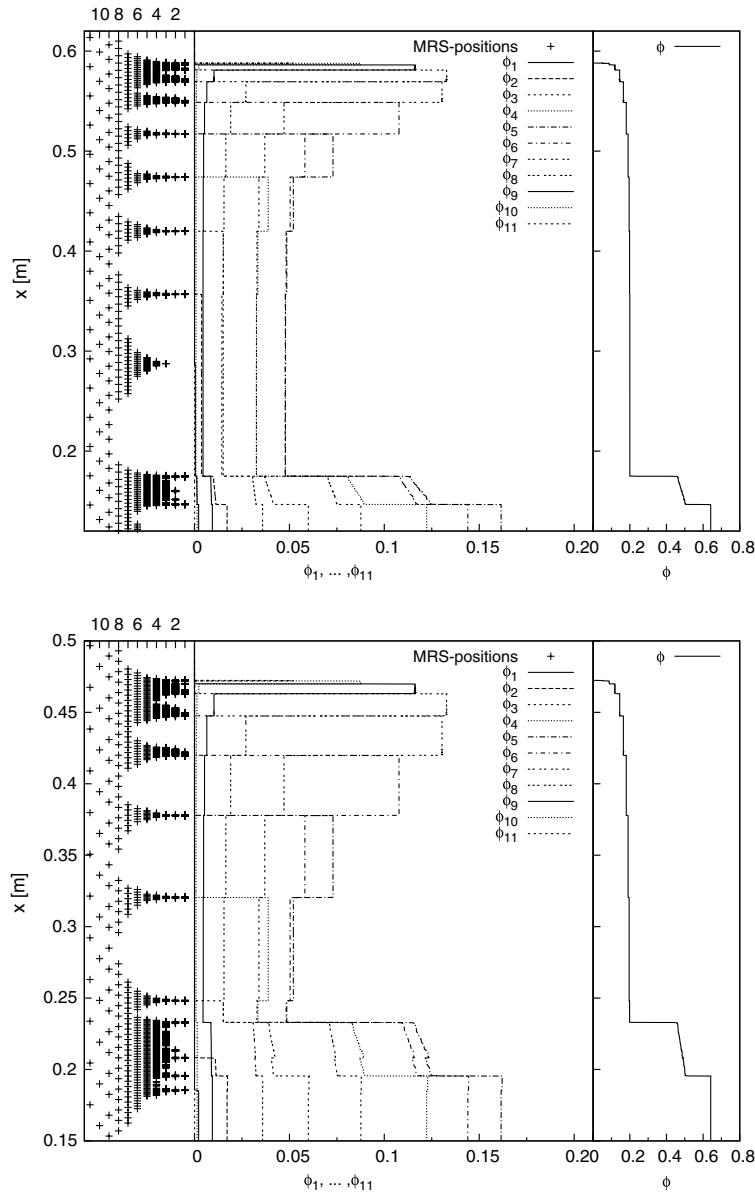

Fig. 21. Example 6 (sedimentation model, $N = 11$): simulation of the settling of a suspension of equal-density particles at $t = 247.77$ s (top) and $t = 330.36$ s (bottom).
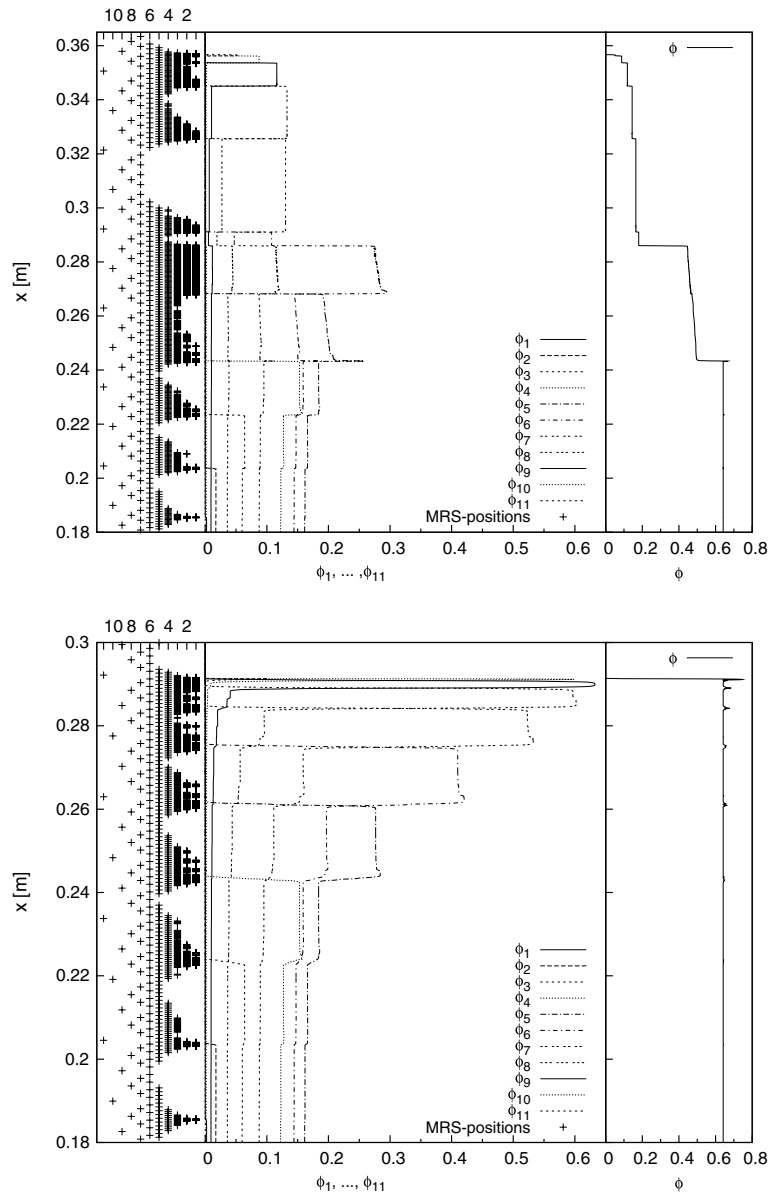
Fig. 22. Example 6 (sedimentation model, $N = 11$): simulation of the settling of a suspension of equal-density particles at $t = 412.94$ s (top) and $t = 578.15$ s (bottom).

For this case, the coarsest and finest grids have 2^5 and 2^{15} points, respectively. The threshold values are $\varepsilon_0 = 10^{-6}$, $\varepsilon_k = 2.5\varepsilon_{k-1}$ and $\theta_k = 2.5\varepsilon_k$, $k = 1,\ldots,L_c$ and CFL $= 0.07$ for both cases.

The solution at five different times is shown in Figs. 21–23, together with the corresponding sets of significant positions, while Fig. 24 displays the evolution of the number of significant positions. Note that the vertical axes in Fig. 22 and 23 have been reduced to segments where interesting features of the solution appear; above and below these segments, the solution is simply obtained by constant extrapolation.

The initial concentrations displayed in Table 3 vary over several orders of magnitude, as do the strengths of the kinematic shocks appearing in the solution. All of them are captured by the multiresolution method. This example has been included as an example of the kind of real-world problem one would probably like to solve by the WENO-MRS method. Nevertheless, one desirable property of any numerical scheme for practical
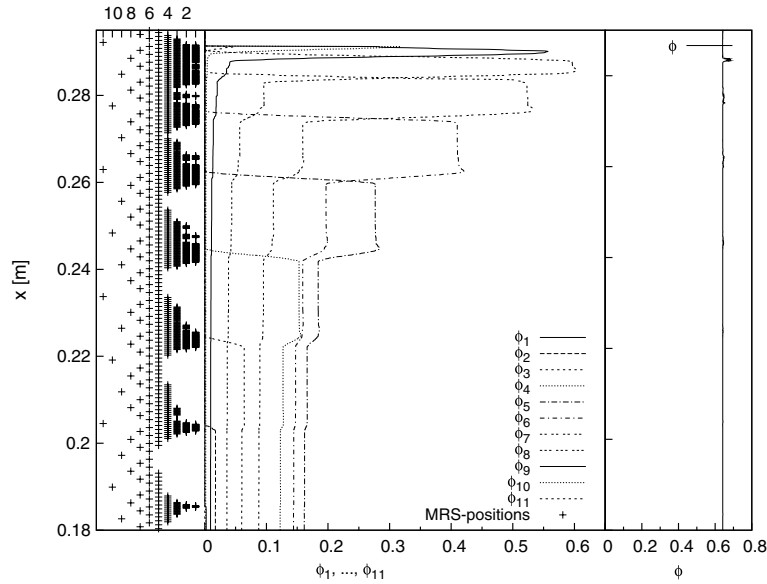
Fig. 23. Example 6 (sedimentation model, $N = 11$): simulation of the settling of a suspension of equal-density particles at time $t = 826$ s.
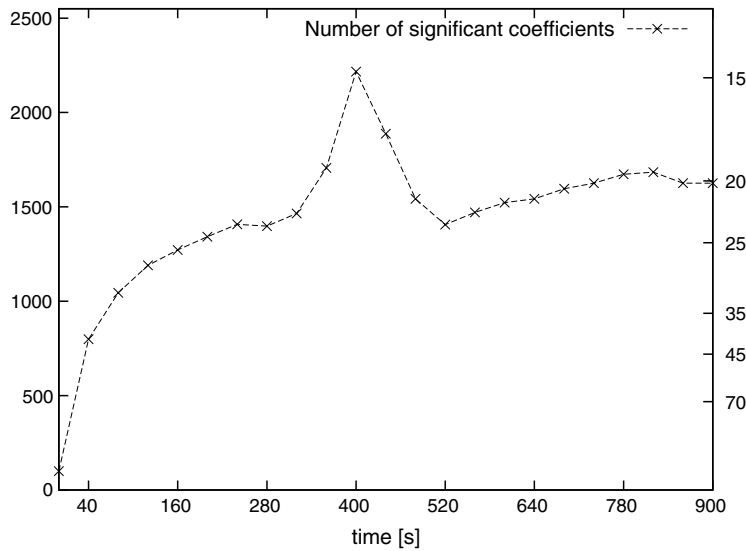

Fig. 24. Example 6 (sedimentation model, $N = 11$): number of significant wavelet coefficients per iteration, with compression rates indicated on the right vertical axis.

applications is that the solution vectors of a kinematic flow problem should remain in the set $\mathscr{E}_{\phi_{max}}$ of physically relevant N-component vectors. Even though we here cut the factor $V(\phi)$ on the boundary $\phi = \phi_{max}$ of $\mathscr{E}_{\phi_{max}}$, this property is not ensured a priori by the present scheme and many other schemes. Actually, this property has so far been ensured for the Lax–Friedrichs scheme only under certain (mild) additional restrictions on $\mathscr{E}_{\phi_{max}}$, see [19]. Though all numerical solution components of our example are nonnegative everywhere, we observe in the ϕ portraits in Fig. 22 that although we have $\phi = \phi_{max}$ in the interior of each sediment layer, near the kinematic shocks separating these layers we have narrow zones where the maximum concentration is slightly exceeded. These numerical artifacts seem to disappear at later times due to slight numerical diffusion (as can be seen in Figs. 23), but they are distracting, and future refinements of the method presented herein may be directed towards avoiding them a priori.

In some of our examples, numerical diffusion still seems to affect the sharpness of resolution of steady-state shocks. This becomes particularly visible if one compares the plots of Fig. 22 with that of Fig. 23. Nevertheless, this phenomenon is not directly related to the multiresolution technique, but is a well-known general consequence of applying universal numerical schemes to stationary data. We should emphasize, however, that the sharpness of shock resolution visible in our Examples 3 and 4 compares favourably with the quite diffusive numerical results obtained for the same cases in [9] by the Nessyahu–Tadmor [34] method.

Finally, we refer back to the comment stated towards the end of Section 2.3. We see that in the sediment zone all concentrations should sum up to $\phi = \phi_{max}$, so that ϕ is constant in that zone, but the sediment includes steady-state shocks which require local grid refinement (i.e., a small scale of the SPR). The WENO-MRS method appropriately generates this refinement, since the set of significant positions is determined according to the local smoothness of each component $\phi_1, \ldots, \phi_N$. In this situation, the refinement would probably not have been generated if we had used ϕ as a smoothness indicator (i.e., as the variable evaluated by Algorithm 2.1), since ϕ (at least in the exact solution) is constant in the sediment zone. This point elucidates that ϕ does *not* contain the singularities of all species.

Acknowledgments

References

[1] G.K. Batchelor, R.W. Janse van Rensburg, Sedimentation in a dilute polydisperse system of interacting spheres, J. Fluid Mech. 119 (1982) 379–408.
[2] S. Benzoni-Gavage, R.M. Colombo, An *n*-populations model for traffic flow, Eur. J. Appl. Math. 14 (2003) 587–612.
[3] M. Berger, J. Oliger, Adaptive mesh refinement for hyperbolic partial differential equations, J. Comput. Phys. 53 (1984) 484–512.
[4] S. Berres, Modeling, analysis and numerical simulation of polydisperse suspensions, Doctoral thesis, University of Stuttgart, 2006.
[5] S. Berres, R. Bürger, K.H. Karlsen, E.M. Tory, Strongly degenerate parabolic–hyperbolic systems modeling polydisperse sedimentation with compression, SIAM J. Appl. Math. 64 (2003) 41–80.
[6] S. Berres, R. Bürger, E.M. Tory, On mathematical models and numerical simulation of the fluidization of polydisperse suspensions, Appl. Math. Modelling 29 (2005) 159–193.
[7] B.L. Bihari, A. Harten, Application of generalized wavelets: a multiresolution scheme, J. Comp. Appl. Math. 61 (1995) 275–321.
[8] B.L. Bihari, A. Harten, Multiresolution schemes for the numerical solution of 2-D conservation laws I, SIAM J. Sci. Comput. 18 (1997) 315–354.
[9] R. Bürger, F. Concha, K.-K. Fjelde, K.H. Karlsen, Numerical simulation of the settling of polydisperse suspensions of spheres, Powder Technol. 113 (2000) 30–54.
[10] R. Bürger, K.-K. Fjelde, K. Höfler, K.H. Karlsen, Central difference solutions of the kinematic model of settling of polydisperse suspensions and three-dimensional particle-scale simulations, J. Eng. Math. 41 (2001) 167–187.
[11] R. Bürger, K.H. Karlsen, E.M. Tory, W.L. Wendland, Model equations and instability regions for the sedimentation of polydisperse suspensions of spheres, ZAMM Z. Angew. Math. Mech. 82 (2002) 699–722.
[12] R. Bürger, A. Kozakevicius, M. Sepúlveda, Multiresolution schemes for strongly degenerate parabolic equations, Numer. Meth. Partial Diff. Eqns., in press.
[13] G. Chiavassa, R. Donat, Point value multiscale algorithms for 2D compressive flows, SIAM J. Sci. Comput. 23 (2001) 805–823.
[14] G. Chiavassa, R. Donat, S. Müller, Multiresolution-based adaptive schemes for hyperbolic conservation laws, in: T. Plewa, T. Linde, V.G. Weiss (Eds.), Adaptive Mesh Refinement—Theory and Applications, Lecture Notes in Computational Science and Engineering, vol. 41, Springer-Verlag, Berlin, 2003, pp. 137–159.
[15] A. Cohen, S.M. Kaber, S. Müller, M. Postel, Fully adaptive multiresolution finite volume schemes for conservation laws, Math. Comp. 72 (2001) 183–225.
[16] C.M. Dafermos, Hyperbolic Conservation Laws in Continuum Physics, second ed., Springer-Verlag, Berlin, 2005.
[17] W. Dahmen, B. Gottschlich-Müller, S. Müller, Multiresolution schemes for conservation laws, Numer. Math. 88 (2001) 399–443.
[18] D.L. Donoho, Interpolating wavelet transforms, Technical Report 408, Department of Statistics, Stanford University, Nov. 1992.
[19] H. Frid, Invariant regions under difference schemes for conservation laws, Discr. Cont. Dyn. Syst. 1 (1995) 585–593.
[20] E. Fried, B.C. Roy, Gravity-induced segregation of cohesionless granular mixtures, in: K. Hutter, N. Kirchner (Eds.), Dynamic Response of Granular and Porous Materials Under Large and Catastrophic Deformations, Springer-Verlag, Berlin, 2003, pp. 393–421.
[21] H.P. Greenspan, M. Ungarish, On hindered settling of particles of different sizes, Int. J. Multiphase Flow 8 (1982) 587–604.

[22] A. Harten, Multiresolution algorithms for the numerical solution of hyperbolic conservation laws, Comm. Pure Appl. Math. 48 (1995) 1305–1342.

[23] A. Harten, Multiresolution representation of data: a general framework, SIAM J. Numer. Anal. 33 (1996) 1205–1256.

[24] M. Holmström, Solving hyperbolic PDEs using interpolating wavelets, SIAM J. Sci. Comp. 21 (1999) 405–420.

[25] L. Jameson, A wavelet-optimized, very high order adaptive grid and order numerical method, SIAM J. Sci. Comput. 19 (1998) 1980–2013.

[26] A.J. Kozakevicius, Wavelets interpolatórias como ferramenta na resolução adaptativa de EDPs hiperbólicas, Ph.D. thesis, IME, Universidade de São Paulo, Brazil, 2002.

[27] A. Kurganov, E. Tadmor, New high resolution central schemes for nonlinear conservation laws and convection–diffusion equations, J. Comput. Phys. 160 (2000) 241–282.

[28] G.J. Kynch, A theory of sedimentation, Trans. Faraday Soc. 48 (1952) 166–176.

[29] R.J. Le Veque, Finite Volume Methods for Hyperbolic Problems, Cambridge University Press, Cambridge, UK, 2002.

[30] M.J. Lighthill, G.B. Whitham, On kinematic waves. II. A theory of traffic flow on long crowded roads, Proc. Roy. Soc. London Ser. A 229 (1955) 317–345.

[31] M.J. Lockett, K.S. Bassoon, Sedimentation of binary particle mixtures, Powder Technol. 24 (1979) 1–7.

[32] J.H. Masliyah, Hindered settling in a multiple-species particle system, Chem. Eng. Sci. 34 (1979) 1166–1168.

[33] H. Moritomi, T. Iwase, T. Chiba, A comprehensive interpretation of solid layer inversion in liquid fluidised beds, Chem. Eng. Sci. 37 (1982) 1751–1757.

[34] H. Nessyahu, E. Tadmor, Non-oscillatory central differencing for hyperbolic conservation laws, J. Comput. Phys. 87 (1990) 408–463.

[35] P.I. Richards, Shock waves on the highway, Oper. Res. 4 (1956) 42–51.

[36] F. Rosso, G. Sona, Gravity-driven separation of oil–water dispersions, Adv. Math. Sci. Appl. 11 (2001) 127–151.

[37] O. Roussel, K. Schneider, A. Tsigulin, H. Bockhorn, A conservative fully adaptive multiresolution algorithm for parabolic PDEs, J. Comp. Phys. 188 (2003) 493–523.

[38] W. Schneider, G. Anestis, U. Schaflinger, Sediment composition due to settling of particles of different sizes, Int. J. Multiphase Flow 11 (1985) 419–423.

[39] P.T. Shannon, E. Stroupe, E.M. Tory, Batch and continuous thickening, Ind. Eng. Chem. Fund. 2 (1963) 203–211.

[40] C.-W. Shu, Essentially non-oscillatory and weighted essentially non-oscillatory schemes for hyperbolic conservation laws, in: B. Cockburn, C. Johnson, C.-W. Shu, E. Tadmor (Eds.), Advanced Numerical Approximation of Nonlinear Hyperbolic Equations, in: A. Quarteroni (Ed.), Lecture Notes in Mathematics, vol. 1697, Springer-Verlag, Berlin, 1998, pp. 325–432.

[41] T.N. Smith, The sedimentation of particles having a dispersion of sizes, Trans. Inst. Chem. Engrs. 44 (1966) 153–157.

[42] Y. Stiriba, S. Müller, Fully adaptive multiscale schemes for conservation laws employing locally varying time stepping, J. Sci. Comp., in press.

[43] E.F. Toro, Riemann Solvers and Numerical Methods for Fluid Dynamics, third ed., Springer-Verlag, Berlin, in press.

[44] E.M. Tory, R.A. Ford, M. Bargieł, Simulation of the sedimentation of monodisperse and polydisperse suspensions, in: W.L. Wendland, M. Efendiev (Eds.), Analysis and Simulation of Multifield Problems, Springer-Verlag, Berlin, 2003, pp. 343–348.

[45] R.H. Weiland, Y.P. Fessas, B.V. Ramarao, On instabilities arising during sedimentation of two-component mixtures of solids, J. Fluid Mech. 142 (1984) 383–389.

[46] G.C.K. Wong, S.C. Wong, A multi-class traffic flow model—an extension of LWR model with heterogeneous drivers, Transp. Res. A 36 (2002) 827–841.

[47] B. Xue, Y. Sun, Modeling of sedimentation of polydisperse spherical beads with a broad size distribution, Chem. Eng. Sci. 58 (2003) 1531–1543.

[48] A. Zeidan, S. Rohani, A. Bassi, P. Whiting, Review and comparison of solids settling velocity models, Rev. Chem. Eng. 19 (2003) 473–530.

[49] M. Zhang, C.-W. Shu, G.C.K. Wong, S.C. Wong, A weighted essentially non-oscillatory numerical scheme for a multi-class Lighthill–Whitham–Richards traffic flow model, J. Comput. Phys. 191 (2003) 639–659.

[50] P. Zhang, R.-X. Liu, S.C. Wong, S.-Q. Dai, Hyperbolicity and kinematic waves of a class of multi-population partial differential equations, Eur. J. Appl. Math. 17 (2006) 171–200.

[51] P. Zhang, S.C. Wong, C.-W. Shu, A weighted essentially non-oscillatory numerical scheme for a multi-class traffic flow model on an inhomogeneous highway, J. Comput. Phys. 212 (2006) 739–756.